



1 **Characterisation of fault plane and coseismic slip for the May 2, 2020,** 2 **Mw 6.6 Cretan Passage earthquake from tide-gauge tsunami data and** 3 **moment tensor solutions**

4 Enrico Baglione^{1,2}, Stefano Lorito², Alessio Piatanesi², Fabrizio Romano², Roberto Basili², Beatriz
5 Brizuela², Roberto Tonini², Manuela Volpe², Hafize Basak Bayraktar^{3,2}, Alessandro Amato²

6 ¹Istituto Nazionale di Oceanografia e di Geofisica Sperimentale (OGS)- Sgonico (TS) – Italy

7 ²Istituto Nazionale di Geofisica e Vulcanologia, Sezione di Roma 1, Via di Vigna Murata 605, 00143, Roma, Italy

8 ³Department of Physics “Ettore Pancini”, University of Naples Federico II, Naples, 80126, Italy

9
10 *Correspondence to:* Enrico Baglione (enrico.baglione@ingv.it)

11 **Abstract.** We present a source solution for the tsunami generated by the Mw 6.6 earthquake that occurred on May 2, 2020,
12 about 80 km offshore south of Crete, in the Cretan Passage, on the shallow portion of the Hellenic Arc Subduction Zone
13 (HASZ). The tide-gauges recorded this local tsunami on the southern coast of Crete island and Kasos island. We used these
14 tsunami observations to constrain the geometry and orientation of the causative fault, the rupture mechanism and the slip
15 amount. We first modelled an ensemble of synthetic tsunami waveforms at the tide-gauge locations, produced for a range of
16 earthquake parameter values as constrained by some of the available moment tensor solutions. We allow for both a splay and
17 a back-thrust fault, corresponding to the two nodal planes of the moment tensor solution. We then measured the misfit between
18 the synthetic and the observed marigrams for each source parameter set. Our results identify the shallow steeply-dipping back-
19 thrust fault as the one producing the lowest misfit to the tsunami data. However, a rupture on a lower angle fault, possibly a
20 splay fault, with a sinistral component due to the oblique convergence on this segment of the HASZ, cannot be completely
21 ruled out. This earthquake reminds us that the uncertainty regarding potential earthquake mechanisms at a specific location
22 remains quite significant. In this case, for example, it is not possible to anticipate if the next event will be one occurring on the
23 subduction interface, on a splay fault, or on a back-thrust which seems the most likely for the event under investigation. This
24 circumstance bears important consequences because back-thrust and splay faults might enhance the tsunamigenic potential
25 with respect to the subduction interface due to their steeper dip. Then, these results are relevant for tsunami forecasting both
26 in the framework of the long-term hazard assessment and of the early warning systems.

27



28 **1 Introduction**

29 On May 2, 2020, at 12:51:07 UTC, a strong earthquake occurred in the Cretan Passage, about 80 km offshore to the south of
30 Crete Island in the eastern Mediterranean. According to the revised moment tensor solution distributed by the GEOFON
31 (<https://geofon.gfz-potsdam.de/>), the earthquake was located at 25.75°E and 34.27°N, at a depth of 10 km, and the moment
32 magnitude (M_w) was 6.6 (Figure 1). Within about 10-15 minutes after the event, estimates of the earthquake magnitude varied
33 from M_w 6.5 to 6.7. This appears, for example, from tsunami alerts issued by the three Tsunami Service Providers (TSPs) of
34 the Tsunami Early Warning and Mitigation System in the North-eastern Atlantic, the Mediterranean and connected seas
35 (NEAMTWS, <http://www.ioc-tsunami.org/>), in charge for monitoring this region: the Centro Allerta Tsunami - Istituto
36 Nazionale di Geofisica e Vulcanologia (CAT-INGV), the National Observatory of Athens (NOA), and the Kandilli
37 Observatory and Earthquake Research Institute (KOERI). These estimates were then confirmed by the moment tensor solutions
38 which started to appear immediately after (Figure 2a).

39
40 The 2020 Cretan Passage earthquake generated a local tsunami along the south-eastern coast of Crete, as reported by
41 eyewitnesses and local authorities and documented by a series of pictures and video shootings taken by authorities, press, and
42 amateurs at Arvi and Kastro villages (Papadopoulos et al., 2020). The NOA-04 tide-gauge station, located in the port of
43 Ierapetra, recorded a peak-to-trough excursion exceeding 30 cm, with a positive peak amplitude of about 20 cm recorded 23
44 minutes after the earthquake origin time, with a wave period of ~3.5 minutes. Small tsunami waves (less than 10 cm peak-to-
45 trough) were also recorded at the NOA-03 tide-gauge, located in the Kasos Island, where the peak amplitude of 5 cm was
46 recorded at 13:53 UTC, and the wave period was estimated to be 8 minutes by Papadopoulos et al. (2020) and 4.5 minutes by
47 Heidarzadeh and Gusman (2021). As in the M_w 6.4, July 1, 2009, event (Bocchini et al., 2020), the tsunami was also observed
48 in the Chrysi islet (located offshore south of Ierapetra), where no tide-gauges are operating. No casualties, injuries or damage
49 were reported due to the tsunami.

50
51 The 2020 Cretan Passage earthquake occurred in the Hellenic Arc Subduction Zone (HASZ). The HASZ is the active plate
52 boundary that accommodates the convergence of the African (or Nubia) plate sinking under the Aegean plate. The arc stretches
53 NW-SE from Kefalonia-Lefkada to Crete and SW-NE from Crete to Rhodes. According to GPS velocities, the relative motion
54 across the HASZ is ~30 mm/y in the NE-SW direction (Nocquet, 2012). The HASZ is characterised by an active volcanic arc
55 in the southern Aegean Sea, an outer non-volcanic arc marking the transition from back-arc extension to contraction in the
56 forearc along the Ionian Islands, Crete, and Rhodes (backstop), a complex accretionary wedge characterised by alternating
57 forearc basins, known as part of the Hellenic Trench (or Trough) System (Matapan, Poseidon, Pliny, and Strabo basins, Fig.
58 1) and Inner Ridges, and the more external, thicker, and wider, Mediterranean Ridge. The accretionary wedge extends above
59 the oceanic crust for more than 200 km, with its leading-edge affecting the remaining abyssal plains (Ionian, Sirte, and
60 Herodotus) and nearing the African continental margin (Polonia et al., 2002; Kopf et al., 2003; Chamot-Rooke et al., 2005;



61 Yem et al., 2011) and has an outward growth rate of 5-20 mm/y (Kastens, 1991). According to reconstructions based on seismic
62 reflection data, most of the structural characteristics of the Mediterranean Ridge external domain can be explained by the
63 presence of thick Messinian evaporites, whereas the internal structures include both frontal thrusts and back-thrusts
64 (Chaumillon and Mascle, 1997; Kopf et al., 2003). Back-thrusts mainly characterise the transition of the Mediterranean Ridge
65 to the inner domain. Strike-slip motions are also present within the Hellenic Trench system.

66
67 Several strong earthquakes struck this area in the past. The largest documented earthquake is the Mw~8.3 365 CE event that
68 occurred in the central forearc of the subduction zone southwest of Crete (Papazachos et al., 2000; Papazachos and Papazachos,
69 2000; Stiros, 2001). This earthquake generated a devastating tsunami (Guidoboni and Comastri, 1997). Another remarkable
70 event is the Mw~8 earthquake of August 8, 1303, which occurred southeast of Crete island, specifically in the arc portion
71 between Crete and Rhodes (Guidoboni and Comastri, 1997, Papazachos, 1996). This earthquake was probably the cause of a
72 tsunami that affected Alexandria in Egypt (Guidoboni and Comastri, 1997). Other strong tsunamigenic earthquakes in the
73 easternmost Hellenic Arc are the Mw 7.5, May 3, 1481 event (Yolsal-Çevikbilen and Taymaz, 2012) and the Mw 7.5, January
74 31, 1741 (Papadopoulos et al., 2007) one. The occurrence of the 1303, 1481 and 1741 tsunamis is also geologically testified
75 by sediments found on the Dalaman coast (Papadopoulos et al., 2014). Another large tsunamigenic earthquake ($M \sim 7.0-7.5$)
76 occurred near southern Crete on July 1, 1494 (Yolsal-Çevikbilen and Taymaz, 2012). More recently, an earthquake of Mw 7.5
77 occurred on February 9, 1948, near the coast of Karpathos, on the Pliny Trench (Papadopoulos et al., 2007) and, on July 1,
78 2009 (UTC 09:30), a moderate earthquake (Mw 6.5) located in the southern offshore margin of Crete caused a local tsunami
79 of about 0.3 m of wave height (Bocchini et al., 2020).

80
81 Despite the relatively high seismicity documented by decades of investigations in macroseismic and instrumental historical
82 seismology in the eastern Mediterranean, several aspects of the tectonic and geodynamic processes that characterise the
83 Hellenic forearc deserve further investigations. For example, the transition from extension to contraction in the forearc is not
84 well delimited, and even the type of seismogenic activity at the subduction interface is not entirely clear.

85
86 For example, the great 365 CE earthquake has been associated with different crustal faults in the upper plate: a reverse splay
87 fault (Shaw et al., 2008; Shaw and Jackson, 2010; Saltogianni et al., 2020) and, recently, a pair of orthogonal normal faults
88 (Ott et al., 2021). Conversely, it seems that the 1303 event was due to a rupture on the plate interface itself (Papadopoulos,
89 2011; Saltogianni et al., 2020). Two recent earthquakes that occurred near the 2020 Cretan Passage event were attributed to
90 two different mechanisms. The source of the recent Mw 6.5, July 1, 2009, earthquake that triggered a small tsunami was
91 suggested to be a splay fault (Bocchini et al., 2020). The Mw 5.5, March 28, 2008, earthquake that occurred to the south of
92 Crete was instead attributed to a north-dipping low-angle thrust faulting mechanism with a small amount of left-lateral slip
93 component (Shaw and Jackson, 2010; Yolsal-Çevikbilen and Taymaz, 2012) representing the subduction interface.

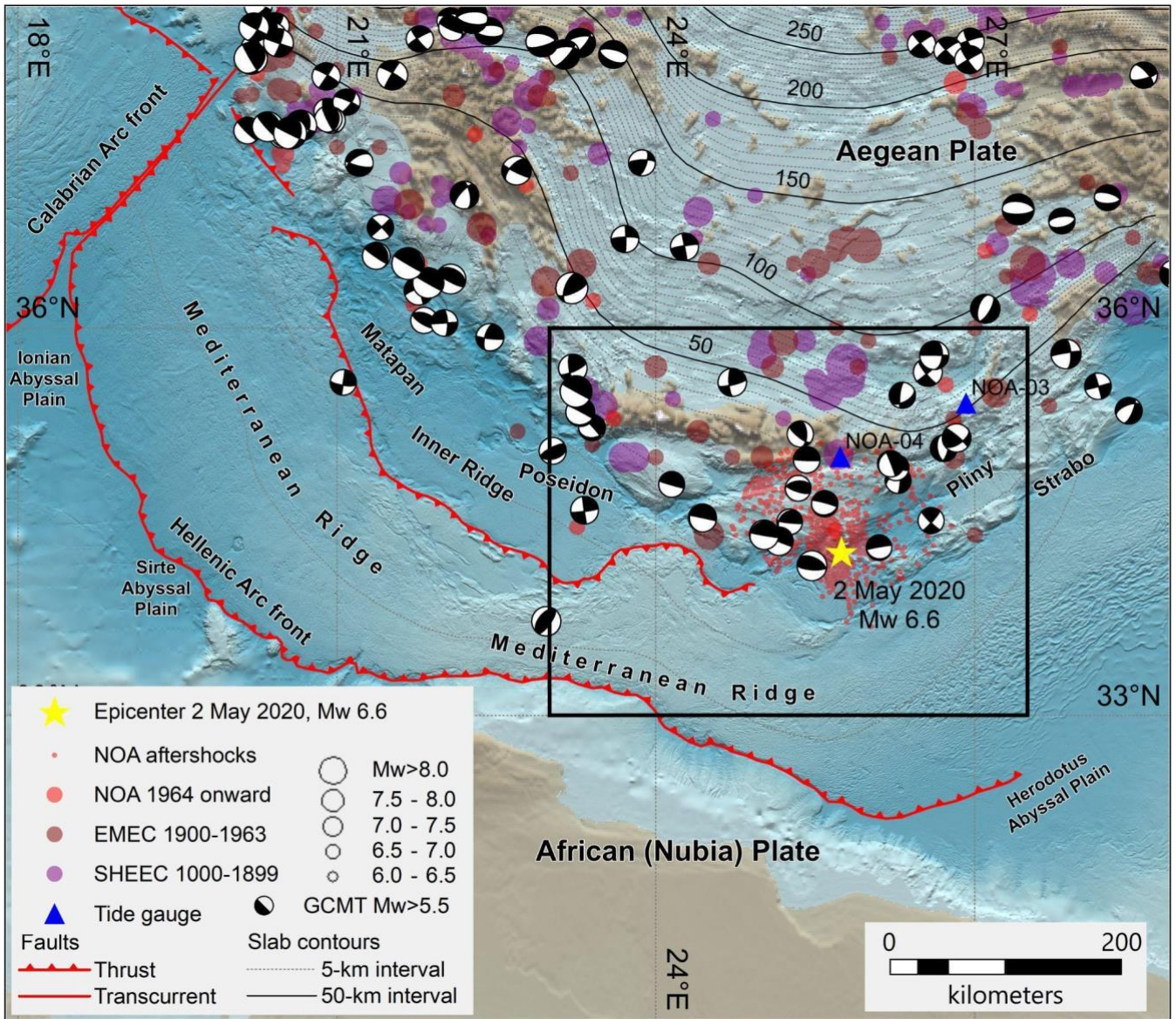


94 Although all the envisaged mechanisms of these examples are consistent with the variety of mechanisms that characterise a
95 subduction zone, the study of the seismogenic and tsunamigenic sources south of Crete remains of key importance for
96 improving the characterisation of the associated hazards, which affects the nearby inhabited coastal areas. This region was
97 already identified as subject to relatively high seismic and tsunami hazard (e.g., Sørensen et al., 2012; Woessner et al., 2015;
98 Basili et al., 2021), and a better characterisation of the potential sources may reduce the uncertainty of such estimates.

99
100 Other authors have already studied the 2020 Cretan Passage event. In particular, Heidarzadeh and Gusman (2021) studied the
101 tsunami source and obtained a heterogenous slip model by inversion and spectral analysis of the tsunami records. They impose
102 a fixed fault geometry for their model, that is one of the two nodal planes (strike, 257° ; dip, 24° ; rake 71°) of the GCMT
103 solution (Dziewonski et al., 1981; Ekström et al., 2012). This solution is a north-dipping plane compatible with a dominantly
104 thrusting mechanism on a splay fault. The fault centre is placed roughly in the middle between the United States Geological
105 Survey (USGS) epicentre (25.712° E, 34.205° N) and the GCMT centroid location (25.63° E, 34.06° N).

106
107 Here, we invert tsunami data for the fault location and orientation (strike and dip angles) as well as for the earthquake-average
108 slip amount and direction (rake angle). To limit the solutions to be explored, we first constrain the parameters to range around
109 the values of the available moment tensor solutions. In this way, while focusing on solutions compatible with the moment
110 tensor inversions of seismic data, we do not exclude a priori that the earthquake might have happened on either nodal planes
111 of these mechanisms. Then, we produce the synthetic tsunami waveforms at the Ierapetra and Kasos tide-gauges for all the
112 sources we obtained. Lastly, we calculate the misfit with observed signals, analyse the misfit distribution for the whole
113 ensemble of models explored, and derive the most likely source model for this earthquake.

114



115

116 **Figure 1:** Main seismotectonic elements of the Hellenic Arc Subduction Zone (HASZ). The seismicity is derived by the SHEEC-EMEC
 117 (Grünthal and Wahlström, 2012; Stucchi et al., 2013) and NOA (<http://www.gein.noa.gr/en/seismicity/earthquake-catalogs>) earthquake
 118 catalogues. Focal mechanisms are from the Global Centroid Moment Tensors database (GCMT; Dziewonski et al., 1981; Ekström et al.,
 119 2012). The slab depth contours are resampled from the European database of Seismogenic Faults (EDSF) (Basili et al., 2013). The topo-
 120 bathymetry is obtained by splicing the ETOPO1 Global Relief Model and EMODnet Digital Bathymetry (DTM 2020) (NOAA, 2009;
 121 Amante and Eakins, 2009; EMODnet Bathymetry Consortium, 2020). The black rectangle outlines the area shown in Figure 2a.



122 2 Data and Methodology

123 We compared the sea level observations at the two tide-gauges (Ierapetra and Kasos) with the synthetic waveforms obtained
124 through numerical tsunami simulations, to identify the source that produced the tsunami based on many different sets of fault
125 parameters. In this section, we describe the technical details of our approach.

126 2.1 Seismic source parameterization

127 We tested different combinations of source parameters, considering 41,310 solutions (Table 1). Each solution is represented
128 by a rectangular fault with uniform slip. The length and width of the fault were assigned based on fault scaling relationships
129 (Leonard, 2014) for a fixed moment magnitude $M_w = 6.6$. We varied position, depth, strike, dip, rake, and slip.

130
131 The earthquake struck in a region where hypocentral locations are usually poorly constrained (Bocchini et al., 2020). The use
132 of a different number of seismic stations, the type of phases used (namely at local, regional or teleseismic distances) and the
133 choice of velocity models can lead to a significant discrepancy in hypocentral locations. The centre of the rectangular fault is
134 thus allowed to span different values of latitude, longitude, and depth (Table 1) to consider this variability.

135
136 Strike, dip, and rake are explored by regular steps within a range of values that envelopes the focal mechanism solutions
137 provided by several agencies (GFZ, USGS, GCMT, IPGP; Figure 2a). Two classes of nodal planes are explored; one is a north
138 shallow-dipping plane, coherently with the dip direction of the subduction interface in that region, or a splay fault (hereafter
139 called “plane S”), the other one is a steep south-dipping plane, likely identifying a back-thrust (“plane B”). Some “extreme”
140 values, like a dip larger than 70° for plane B or lower than 20° for plane S, have been excluded after some preliminary tests, as
141 they were significantly worsening the misfit between synthetic and observed waveforms. Slip is allowed to vary between 0.35
142 and 1.15 m, with a step of 0.05 m.

143
144 **Table 1:** Source parameters variability of the source model dataset for the tsunami simulations. The different sets of focal plane
145 parameters are separated by parenthesis (B and S refer to the back-thrust and splay fault solutions). Positions and depths are referred to the
146 centre of the fault plane.

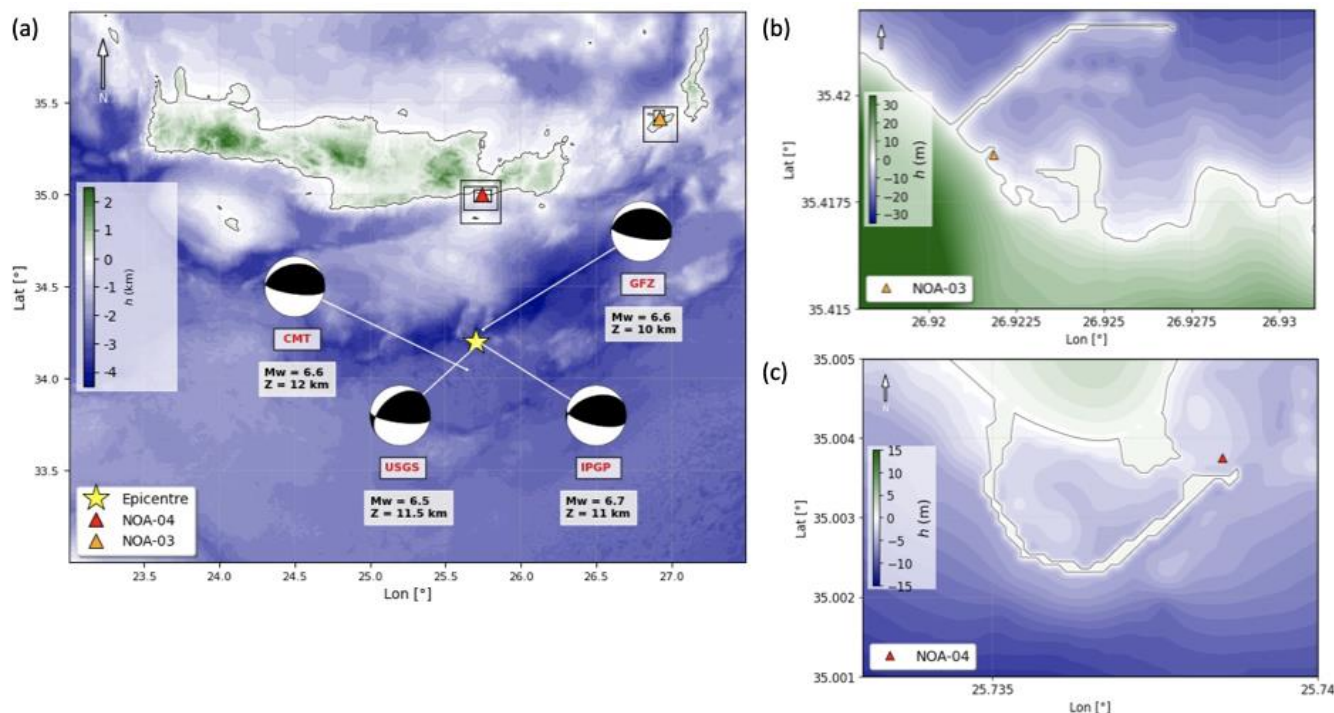
Source parameters	
Length (km)	26.04
Width (km)	15.42
Depth (km)	10; 15; 20
Lat ($^\circ$ N)	34.1; 34.2; 34.3
Lon ($^\circ$ E)	25.6; 25.7; 25.8
Slip (m)	from 0.35 to 1.15, step 0.05
Strike ($^\circ$)	B (95; 105), S (225; 235; 245; 255; 265)



Dip (°)	B (50; 60; 70), S (20; 30; 40)
Rake (°)	B (85; 95; 105; 115, 125), S (45; 55; 65; 75)

147

148



149

150 **Figure 2:** (a) Computational domain for the tsunami modeling adopted in this study (see text for details). The yellow star indicates the
 151 epicentre, at the centre (34.2°N, 25.7°E) of its considered variability range. The different bathymetric levels are plotted as black rectangles.
 152 The red and orange triangles represent the Ierapetra (NOA-04) and Kasos (NOA-03) tide-gauge stations, respectively. The different focal
 153 mechanisms used as reference values to let the inversion parameters vary are plotted, each with its own agency label: GEOFON (GFZ,
 154 <https://geofon.gfz-potsdam.de/>), United States Geological Survey (USGS, <https://earthquake.usgs.gov/>), Institut de Physique du Globe de
 155 Paris (<http://geoscope.ipgp.fr/>), Global CMT Catalog (<https://www.globalcmt.org/>). (b) High-resolution bathymetry data (10 m spatial
 156 resolution) around NOA-03 (Kasos) and (c) NOA-04 (Ierapetra) tide-gauges.

157 2.2 Tide-gauge data and tsunami modelling

158 The tsunami signal recorded by the tide-gauges at Ierapetra (NOA-04) and Kasos (NOA-03) was obtained after removing the
 159 tidal component from the original waveform (<http://www.ioc-sealevelmonitoring.org>, sampling rate of 1 min) through a
 160 LOWESS procedure (e.g., Romano et al., 2015).

161



162 Tsunami numerical modelling was performed with the Tsunami-HySEA software, which uses a finite volumes approach and
163 a nested grid scheme to progressively increase the resolution during the propagation from the source to the tide-gauges. The
164 software has undergone proper benchmarking (Macías et al., 2017) according to the community standards (e.g., Synolakis et
165 al., 2009), also within the framework of the US tsunami hazard program (<http://nws.weather.gov/nthmp/>). The code is
166 implemented in CUDA (Compute Unified Device Architecture) and runs in multi-GPU architectures, yielding remarkable
167 speedups compared to other CPU-based codes (de la Asunción et al., 2013).

168

169 To build the bathymetric and topographic grid models for the simulations, we used: 1) the European Marine Observation and
170 Data Network (EMODnet) project database (EMODnet DTM version released in 2018, <http://portal.emodnet-bathymetry.eu/>),
171 which has a resolution of about 115 m; 2) the European Digital Elevation Model (EU-DEM), version 1.1
172 (eu_dem_v11_E50N10), with a resolution of 25 m; and 3) the nautical charts (<https://hartis.org/en>) of Ierapetra harbour
173 (Ierapetra Bay, 1:10,000 scale; Kaloi Limenes Bay, 1:12,500 scale) and Kasos harbour (Diafani Harbour, 1:5,000 scale; Pigadia
174 Bay and Harbour, 1:5,000 scale; Emporio Harbours, 1:5,000 scale). The computational domain (33-36° N, 23-27.5° E, Figure
175 2a) for tsunami propagation consisted in four levels of nested grids with increasing resolution approaching the Ierapetra and
176 Kasos harbours (640, 160, 40, and 10 m, respectively). The domains of the finest grids are shown in Figures 2b and 2c.

177

178 The instantaneous seafloor vertical displacement was calculated using Volterra's formulation of elastic dislocation theory
179 applied to a rectangular source embedded in an elastic half-space (Okada, 1992), and the initial velocity field is assumed to be
180 zero everywhere. The initial sea surface elevation was obtained by applying a low-pass filter to reproduce the water column
181 attenuation; the filter has a trend of the type $1/\cosh(kh)$, where "k" is the wavenumber, and "h" is the average water depth
182 (Kajiura, 1963).

183

184 We performed 2,430 simulations exploring all the source parameters (Table 1) except for the slip, which is fixed in all runs to
185 1 meter to obtain Green's functions. For all of these scenarios, we simulated one hour of propagation after the earthquake
186 origin time (hereinafter OT) for the Ierapetra station and one hour and 30 minutes of propagation for the Kasos station. These
187 simulation lengths allowed us to have about 50 minutes of tsunami signal at both gauges, which is more than enough to include
188 the first tsunami oscillations (~30 min), that carry the information on the source and are used for the inversion (see Section
189 2.3). Time histories of the tsunami waves were calculated at the wet points of the computational grid closest to the Ierapetra
190 and Kasos station coordinates (see Figure 2) and stored every 60 s, consistently with the actual tide-gauge sampling. We
191 assumed linearity between the slip amount and the tsunami to obtain the scenarios for different slip values. Thus, we multiplied
192 each of the computed marigrams by all the 17 slip values, for a total of 41,310 tsunami realisations.

193



194 2.3 Inversion

195 To retrieve the fault parameters and the coseismic slip simultaneously, we solved a nonlinear inverse problem. Since the
196 number of sources in our ensemble is not very large, we opted for a systematic search of the parameters' space.

197

198 The comparison between the synthetic and the observed waveforms is carried out in the time domain. The misfit between the
199 two waveforms is evaluated through a cost function frequently used to compare tsunami signals in source inversions (e.g.,
200 Romano et al., 2020):

$$201 \quad E = 1 - \frac{\sum_{t_i}^{t_f} \eta(t-T)\eta_o(t)}{\sum_{t_i}^{t_f} \eta^2(t-T) + \sum_{t_i}^{t_f} \eta_o^2(t)}, \quad (1)$$

202 In equation (1) $\eta(t)$ and $\eta_o(t)$ are the synthetic and the observed waveforms, respectively, t_i and t_f are the lower and upper limit
203 of the considered time window, and T is a time shift. The cost function considers both the amplitude and the shape of a
204 waveform; it is more robust than a least-squares misfit, whose solutions are very sensitive to a small number of large errors in
205 the dataset (Tarantola, 1987). For each combination of the source parameters, the cost function is minimised with respect to
206 time shift values between -5 and 5 minutes, with one-minute steps. The arrival time optimisation is used to overcome the often
207 found time alignment mismatch between the observed and modelled tsunami waveforms, with the latter generally arriving
208 earlier. This approach was introduced by Romano et al. (2016), and the details are discussed further in Romano et al. (2020).

209

210 The overall cost function is a weighted average of two cost functions calculated on the two considered tide-gauges. The weights
211 are chosen such that $\frac{w_{NOA-03}}{w_{NOA-04}} = 0.2$, equivalent to the ratio of the maximum tsunami amplitude registered at the two tide-
212 gauges in the first half an hour after the tsunami arrival. Several attempts were made, showing that the results are driven by
213 the Ierapetra contribution for a wide range of weights. The higher sensitivity of the Ierapetra signal to the source details is not
214 surprising, since the Kasos station is much further away from the source, and the associated recorded marigram shows a very
215 low peak-to-trough excursion and a lower signal to noise ratio.

216

217 Time windows of [5, 30] and [30, 55] minutes after the earthquake OT are chosen, respectively, for the Ierapetra and Kasos
218 tide-gauges. This choice was made to include the first tsunami oscillations, which are mainly driven by the seismic source.
219 The remaining part of the records is not used for the inversion, because it is highly probable that other factors, such as the local
220 propagation and the port structure, start to control the shape of the signal (Romano et al., 2016; Cirella et al., 2020). To quantify
221 the relative importance of these factors, the cost function is also evaluated in the 25 minutes following the considered intervals,
222 that is in the time windows [30,55] and [55,80] minutes for Ierapetra and Kasos, respectively. The average of the cost functions
223 (E_1 for [30,55] min., E_2 for [55,80] min.) is calculated from the 5, 10, 50, and 100 percent of models with the lowest misfit E_1
224 (within the first window used for the inversion) with the observed data. We observe that the ratio E_2/E_1 significantly decreases



225 when using progressively more models ($E_2/E_1 = 4.9, 4.5, 3.0, 2.0$, respectively). This observation confirms that the information
226 about the source dominates the first intervals used for the inversion.

227

228 2.4 Synthetic test

229 We first investigated the resolution offered by the two stations using as a target source model all possible combinations of the
230 source parameters $A(a_1, a_1, \dots, a_n)$. These are the same models we explored in the inversion for the real case. For each of them
231 we calculated the corresponding synthetic target waveform and corrupted it by adding a Gaussian random noise with a variance
232 corresponding to the 10% of the clean waveform amplitude variance. A random time shift between -5 and 5 minutes is added
233 to mimic the typically observed time mismatch between the observed and the predicted tsunami signals.

234

235 All the waveforms $f(A)$ derived from all the possible source models are tested against each of these noisy and shifted target
236 waveforms $f_T(A)$ using equation (1). We then defined the distance between two different models as:

$$237 \quad d_{ij} = \frac{\|a_i - a_j\|}{M \cdot \|a_j\|}, \quad (2)$$

238 Where $a_i = (\text{strike, dip, rake, slip, depth, lon, lat})_i$, $a_j = (\text{strike, dip, rake, slip, depth, lon, lat})_j$ are the parameters associated with
239 the i -th (j -th) combination, and M (equal 7) is the number of free parameters.

240

241 For each target model a_i , the distance d is evaluated with respect to:

- 242 1) the best model a_{best} , whose $f(a_{\text{best}})$ presents the lowest cost function;
- 243 2) the average model a_{wm} evaluated as a weighted mean over the first 5% of the models with the lowest cost function,
244 where the weights are chosen as the reciprocal of the cost function.

245

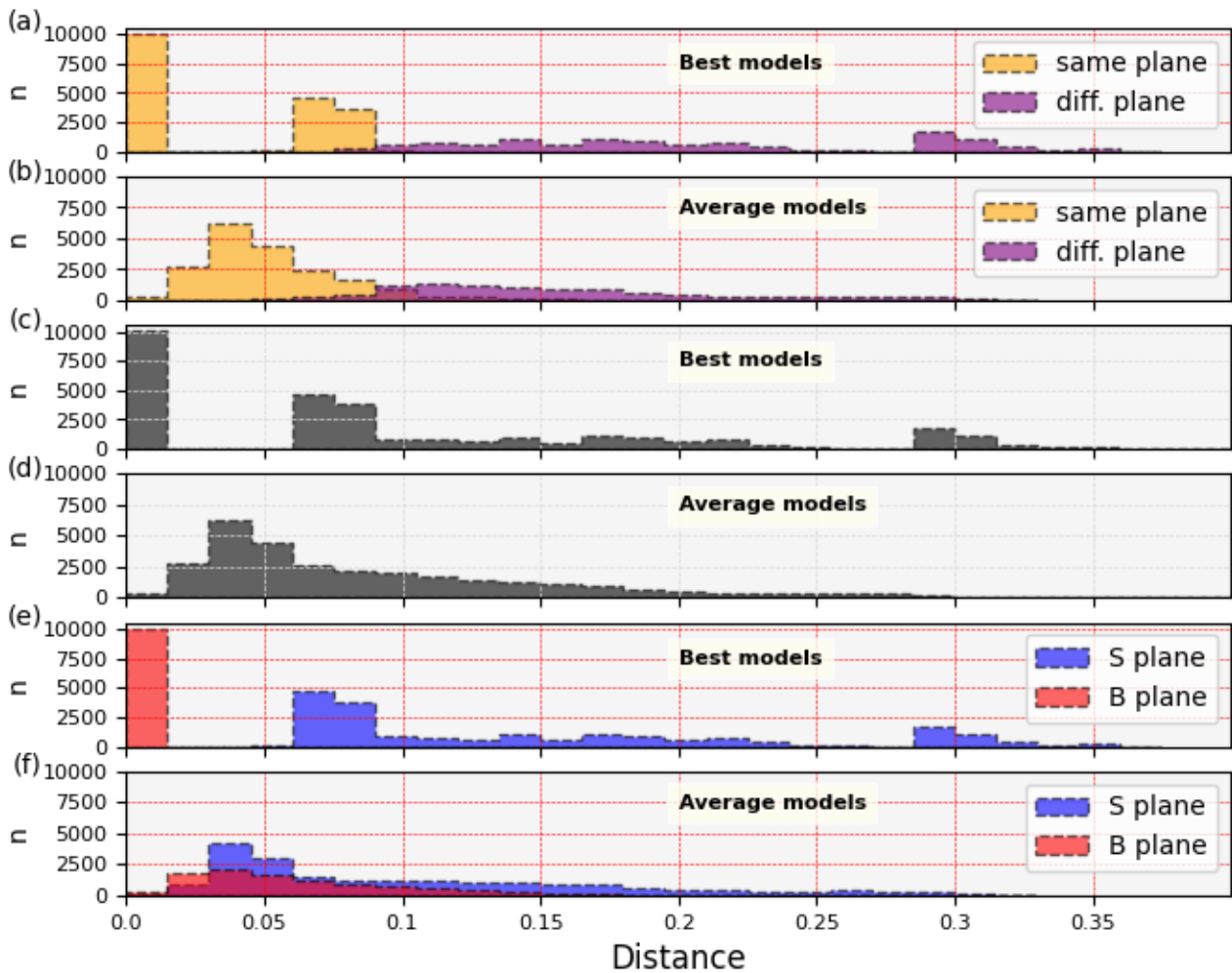
246 The result confirms that the tsunami data well constrain the seismic source process. In most cases, the target parameters
247 correspond to those of the model which minimises the cost function (Figures 3a and 3c). Hence, the target focal plane is
248 correctly identified. The few cases showing a high value of the distance occurs when the algorithm does not recognise if the
249 target is a back-thrust or a splay fault.

250

251 On the one hand, when using the average model, the distance between the models almost never vanishes (Figures 3b and 3d),
252 meaning that the target's parameters are not perfectly reproduced, as expected for an average model. On the other hand, the
253 averaging process has the power to make the distribution smoother and unimodal and to eliminate or diminish the number of
254 occurrences corresponding to a high distance. So, choosing the average over the best models may protect us from overfitting.



255 Figure 3e shows that the B plane (a back-thrust) is much better spotted than the S one (the splay) by the best models; when
256 using the average model, the difference in the “specificity” of the cost function is slightly reduced but still present (Figure 3f).
257



258
259 **Figure 3:** Distributions of the parameters distance for the best (a, c, e subplots) and average models (b, d, f subplots). Subplots (a) and (b)
260 separate the models for which the target model focal mechanism is reproduced or not. Subplots (c) and (d) report all the models together.
261 Subplots (e) and (f) separate the target models associated with the B (red) or S (blue) focal plane solutions.

262 3 Results of the application to the May 2, 2020, Mw 6.6 Cretan Passage earthquake

263 We performed the inversion using the observations at Ierapetra and Kasos, the only two sea level recordings available. The
264 distribution of the cost function values for all the investigated models is shown in Figure 4. Figure 4a displays separately the
265 cost function values obtained for the two focal solutions. Overall, the cost functions of the B plane are slightly lower than those

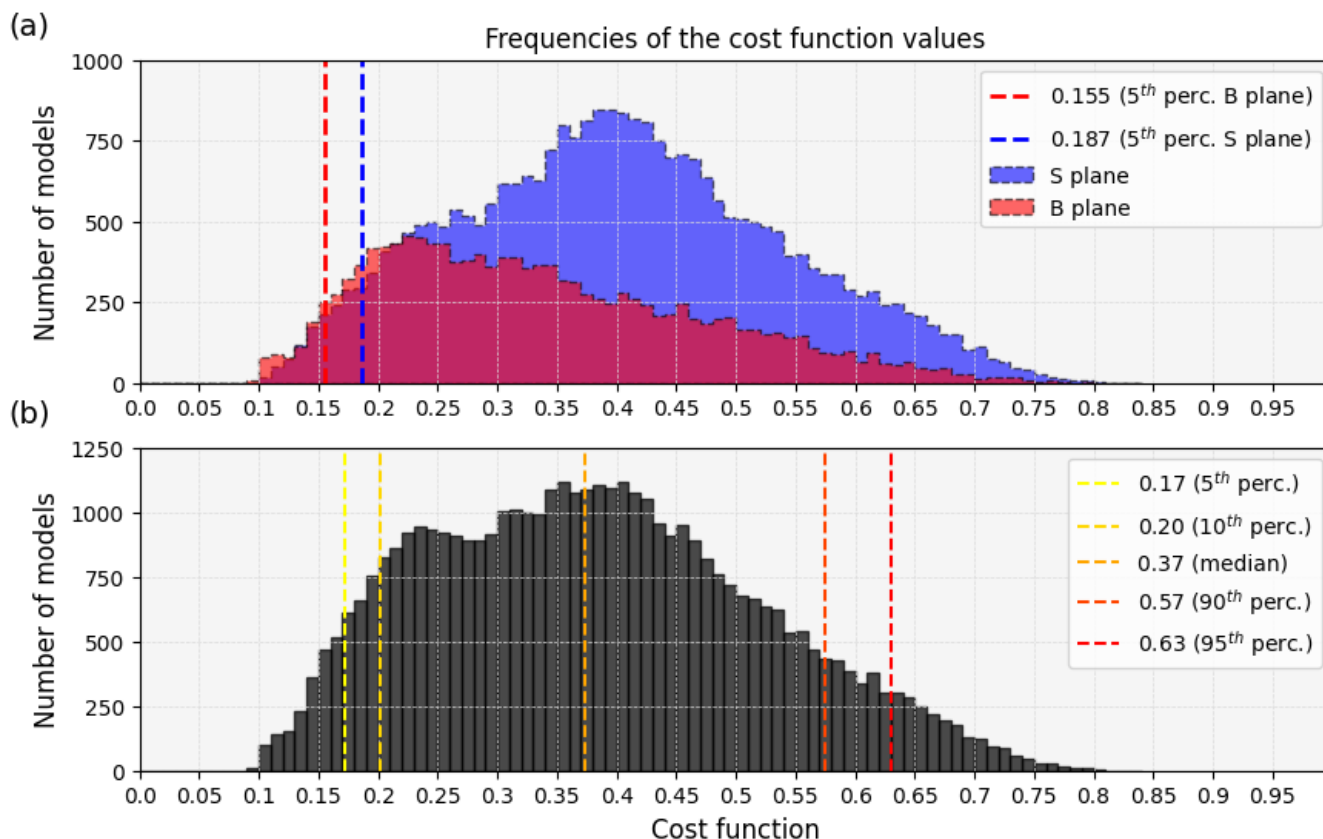


266 of the S plane. However, the left portions of the distributions, that is the ones containing the models with the lowest misfit with
267 respect to the observed marigrams, are almost overlapped. The same tendency can be seen in Figure 4b where the distribution
268 has a slightly bimodal character with the two modes corresponding to the S and B planes, respectively.

269
270 Based on the resolution test results presented in Section 2, we evaluated the weighted average of the models included in the
271 5th percentile of the cost function distribution for each focal solution (those to the left of the dashed lines in Figure 4a). We
272 used as a weight the inverse of the cost function. Both the best and average models, as well as the associated errors obtained
273 as weighted standard deviations, are reported in Table 2.

274
275 The average models, along with the associated errors, may indicate that the best model is “overfitting” the data. This happens,
276 for example, when the best and average models are very different or when the uncertainties are very large. Standard deviations
277 give a measure of the uncertainties in the estimation of the corresponding parameter. Smaller values of the standard deviation
278 denote a parameters’ better resolution (Mosegaard and Tarantola, 1995; Sambridge and Mosegaard, 2002; Piatanesi and Lorito,
279 2007).

280
281
282



283

284 **Figure 4:** (a) Cost function distribution for the back-thrust (red) and the splay (blue) models; the vertical dashed lines indicate the 5th
285 percentiles for each of the two focal solutions. (b) Histogram of the cost function values for all the models considered. The vertical dashed
286 lines represent the 5th, 10th, 50th (median), 90th and 95th percentile.

287

288 With only a few exceptions, all the best model parameters fall within the range of one standard deviation from the average
289 model. For both focal solutions, the slip of the best models is quite smaller than the average one and does not fall within the
290 uncertainty limits.

291

292 The S plane solutions are centred about 10 km north of the B planes, slightly closer to the southern coast of Crete. Coherently,
293 the predicted tsunami arrives earlier (i.e., the estimated time-shift is bigger) with respect to the waves resulting from the B
294 plane solutions. The rake angle, both for B and S planes, presents a large dispersion. The same can be said for the strike
295 associated with the S plane. On the other hand, the dip appears to be better constrained.

296

297

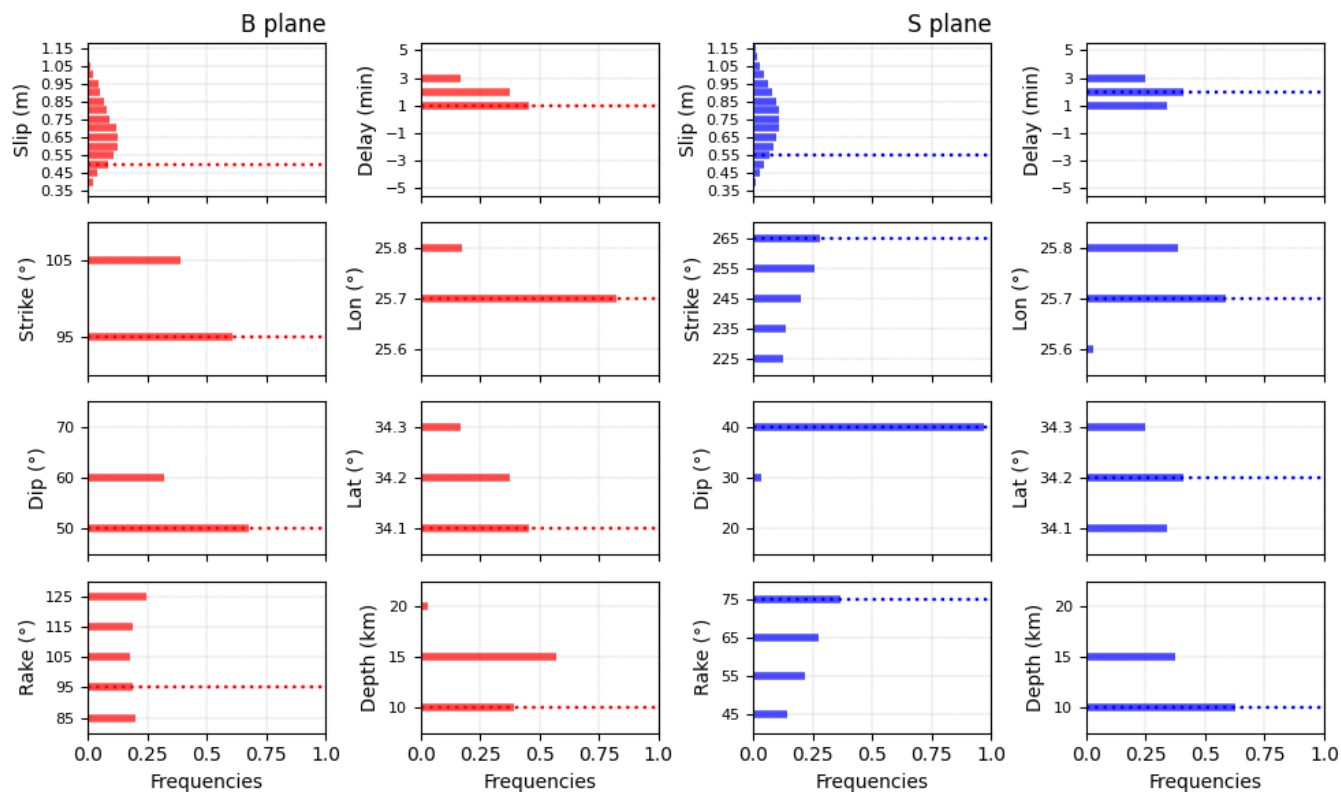


298 **Table 2:** Best and Average Model extracted from the models with the smallest cost functions within the 5th percentile. The percentiles
299 refer to B and S planes separately (i.e., the models at the left of the red and blue vertical dashed lines in Figure 4a, respectively). B plane
300 refers to the back-thrust solution dipping south; S plane refers to the splay fault dipping north. Lat, Lon and Depth refer to the centre of the
301 fault.

	Best model plane B	Average model (5 th) plane B	Best model plane S	Average model (5 th) plane S
Depth (km)	10	13 ± 3	10	12 ± 2
Lat (°N)	34.1	34.17 ± 0.07	34.2	34.19 ± 0.08
Lon (°E)	25.7	25.72 ± 0.04	25.7	25.73 ± 0.05
Strike (°)	95	99 ± 5	255	249 ± 14
Dip (°)	50	53 ± 5	40	39 ± 2
Rake (°)	95	106 ± 15	75	64 ± 11
Slip (m)	0.50	0.68 ± 0.15	0.55	0.75 ± 0.16
Time.shift (min)	1	1.7 ± 0.7	2	1.9 ± 0.8

302
303
304 Figures 5-7 help to visualise the parameter variability and how the best source models are characterised. The marginal (Figure
305 5) and the joint distributions (Figure 6 and 7) are provided for the two planes. Marginal and joint distributions provide an
306 additional measure of the uncertainties. Narrower distributions suggest that the corresponding parameters are better resolved
307 than those characterised by broader ones.

308
309 The strike angle for plane B and the dip angle for plane S show a strongly “preferred” value (diagonals of Figures 6 and 7).
310 The rake angle does not show a real preferential value: evidently, we do not have enough precision to discriminate at this level
311 of resolution. Plane B solutions are characterised by a larger depth dispersion and by a higher average depth value. However,
312 the depth of 20 km almost never occurs, suggesting the occurrence of a shallow event. The slip shows a “bell-shaped”
313 distribution with a peak at 0.65 m and 0.75 m for B and S plane respectively, and significant occurrences in the range 0.50-
314 0.90; the best source slip is lower than the average, both for plane S and B. S plane solutions are characterised by a slightly
315 higher slip than B plane solutions. There is a correlation between the slip and depth values: deeper solutions consistently
316 feature a larger slip. In this case, a lighter correlation also exists between slip and latitude: events further south have a slightly
317 greater slip, especially for B solutions. As regards the hypocentre determination, establishing a univocal position is not obvious,
318 also because the delay adds a trade-off in constraining the hypocentre. Consequently, the Longitude is better constrained than
319 the Latitude since the latter is more strongly correlated with the arrival time given the relative position of the tide-gauges (both
320 to the north) with respect to the source. The preferred longitude is 25.7°E, with fewer occurrences a little further east and
321 almost none further west.



322

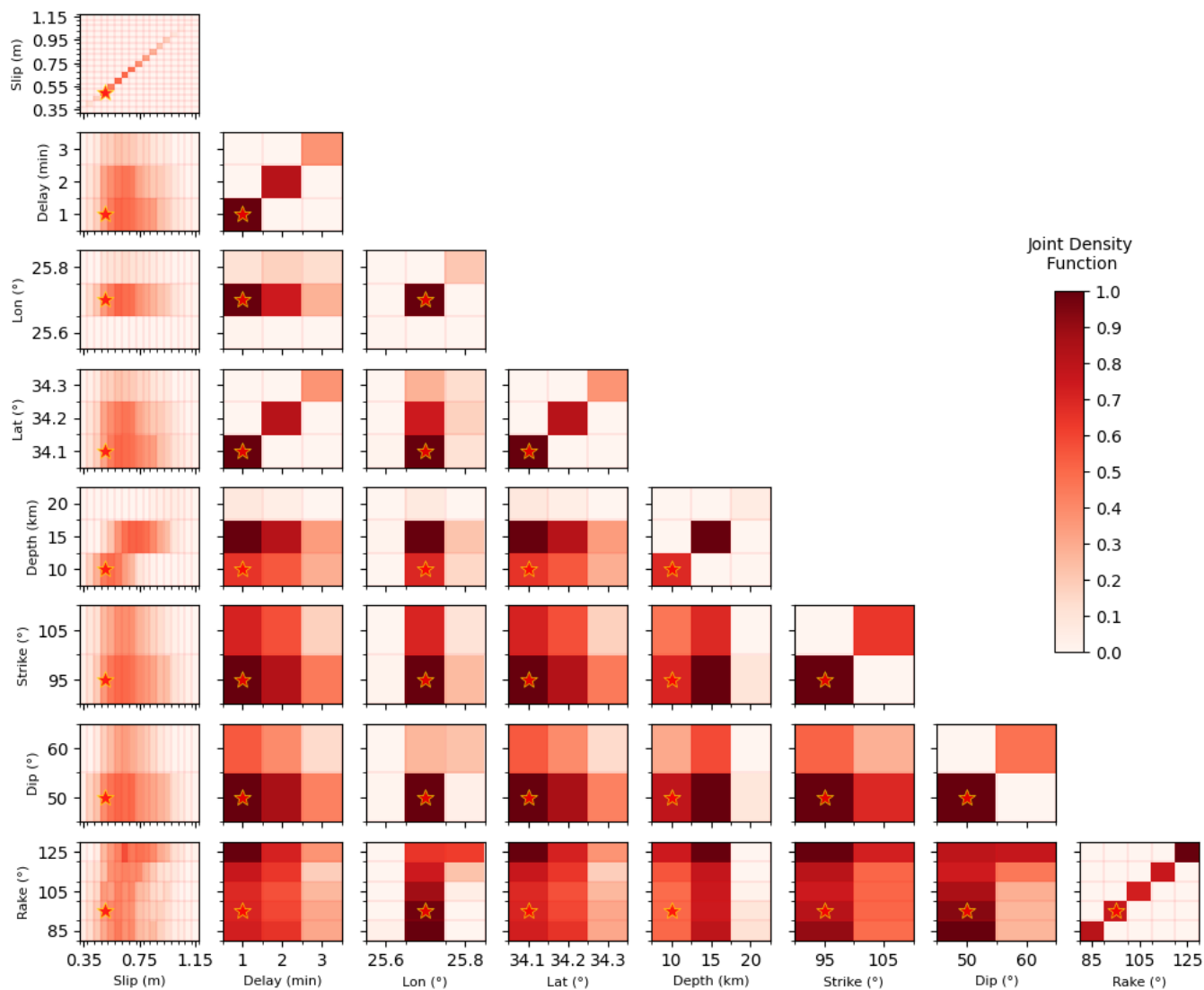
323

324

325

326

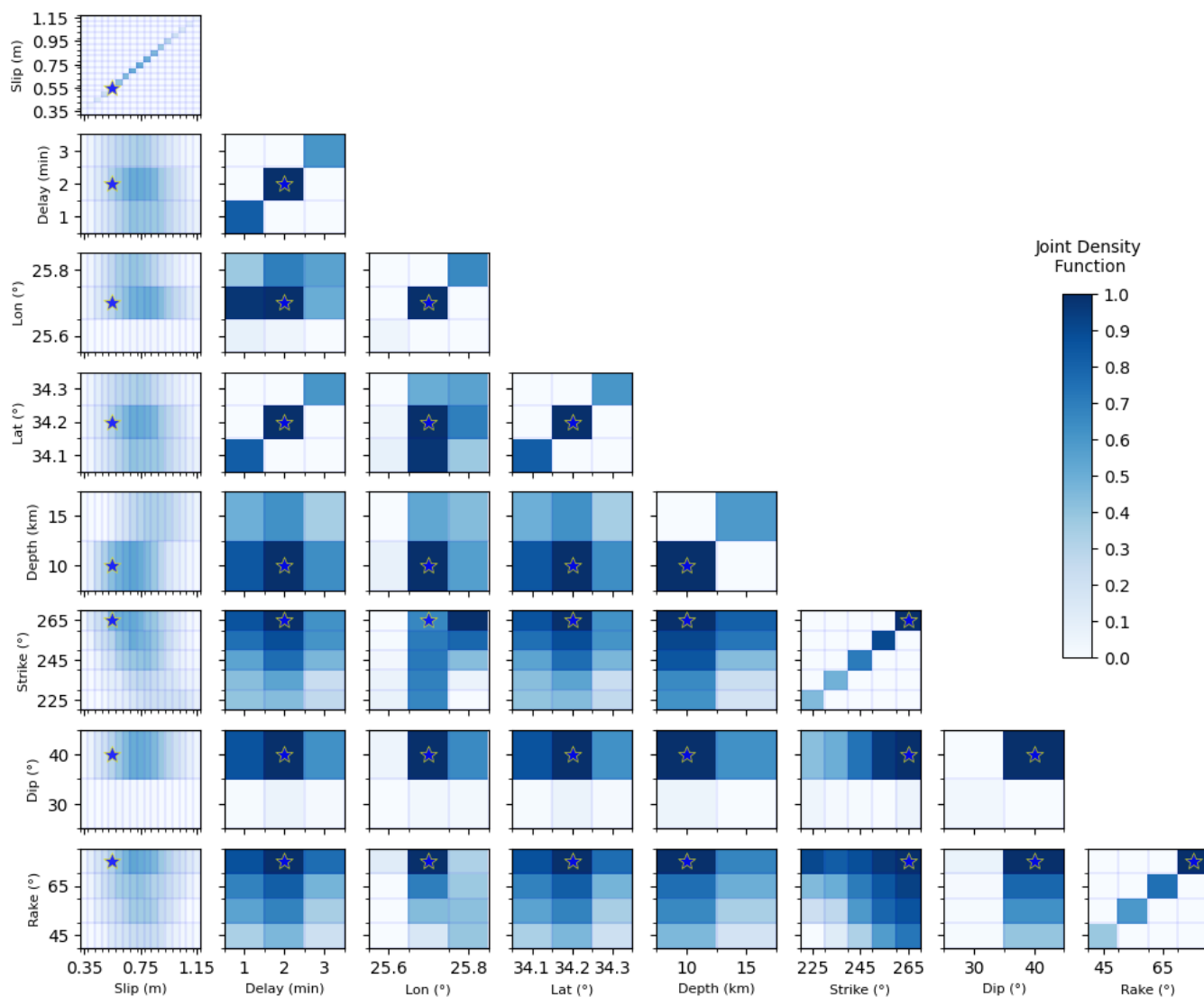
Figure 5: Marginal distributions for each of the inverted parameters, considering the first 5 percent of B (1st and 2nd columns) and S (3rd and 4th columns) plane models, those at the left of the red and blue vertical line in Figure 3a. The red and blue horizontal dotted lines mark the best models for the B and S planes, respectively.



327

328 **Figure 6:** Joint density distribution for each couple of the back-thrust source's parameters, considering the first 5 percent of B plane models,
329 those at the left of the red vertical line in Figure 3a. The red star identifies the best model.

330



331

332 **Figure 7:** Joint density distribution for each couple of the splay source's parameters, considering the first 5 percent of S plane models, those
333 at the left of the blue vertical line in Figure 3a. The blue star identifies the best model.

334

335 The comparison between the observed data and the synthetic ones generated with both the best and the average source models
336 at Ierapetra and Kasos tide-gauge is shown in Figure 8; those corresponding to the two planes B (Figure 8a and e) and S (Figure
337 8c and g) are plotted separately. Both synthetic signals reproduce quite well the first oscillations. It is interesting to note a
338 possible “clipping” of the negative peak of the signal at ~ minute 27 caused by the insufficient sampling frequency. For what
339 concerns the following peak (minute 28), the average signals result instead to be lower, particularly for the B plane.

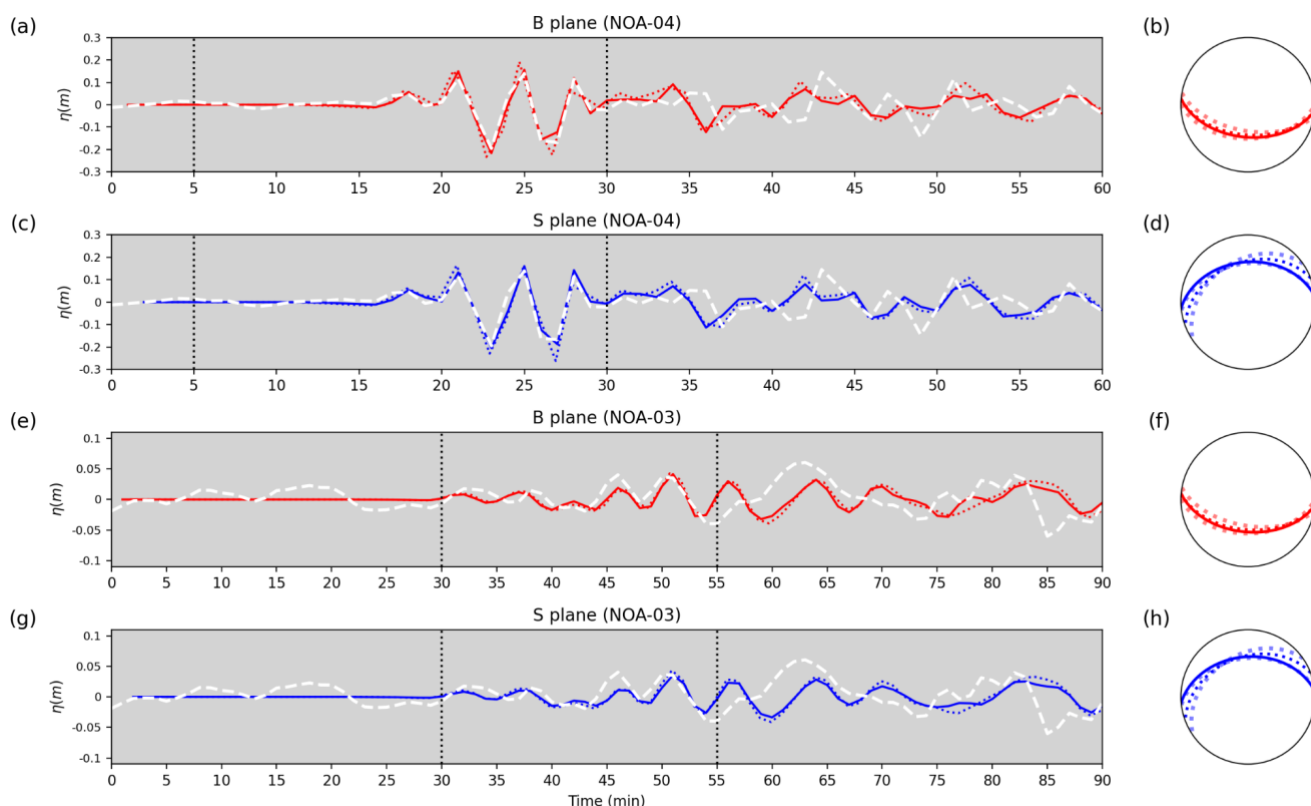
340



341 In terms of wave fitting, the comparison between the data and the predictions of the average models is only slightly worse than
342 that found with the best model. The choice between best and average models for both focal solutions is not sufficient for
343 discriminating, as there are no significant differences, except for the slip, between them. Both can be chosen as the
344 representative of the best sources' ensembles.

345

346



347

348 **Figure 8:** Best (solid lines) and average (dotted lines) marigrams obtained at the two stations. Plots (a) and (c) refer to the Ierapetra tide-
349 gauge (NOA-04) while (e) and (g) to the Kasos one (NOA-03). The white dashed line is the observed water elevation at each tide-gauge. B
350 plane (in red) refers to the back-thrust solution dipping south; S plane (in blue) refers to the splay fault dipping north. The vertical dotted
351 lines indicate the limits of the time window used for the inversion. On the right of each marigram plot the stereonets (lower hemisphere)
352 show the fault orientations corresponding to the best signal (solid line) and the average one (dotted line) with the variability derived from
353 the standard deviations of Table 2.

354

355

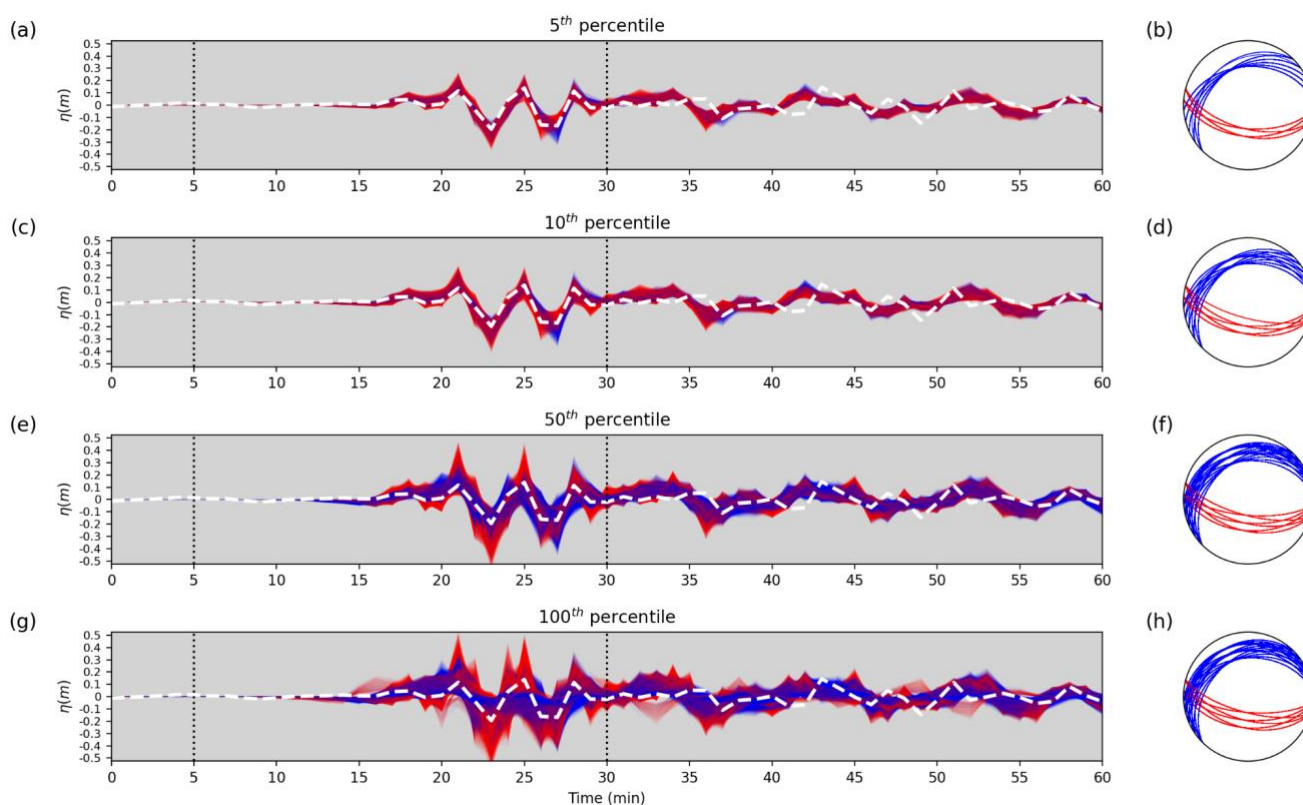


356 The signals belonging to the 5th, 10th, 50th and 100th percentiles of the cost function are shown in Figure 9 (Ierapetra) and
357 Figure 10 (Kasos) to provide a better idea of what a certain cost function implies in terms of waveform fitting with respect to
358 the observed data. Significant discrepancies start to appear when including the models in the 10th percentile and beyond,
359 confirming that all the models with a lower cost function may be equally reasonable solutions.

360
361 The synthetic marigrams at Ierapetra and Kasos reproduce quite well the observed tsunami waveforms for the first cycles of
362 the signal, those carrying most of the source-related information. As discussed above, the agreement worsens as time
363 progresses due to the possibility of not well-modelled propagation complexity around the tide-gauge. After roughly half an
364 hour from the tsunami first arrival, there is a larger and larger deviation between the synthetic and the observed marigrams
365 (Figure 8).

366
367 Overall, the results do not conclusively indicate that one focal plane should be preferred over another, and both solutions
368 remain possible.

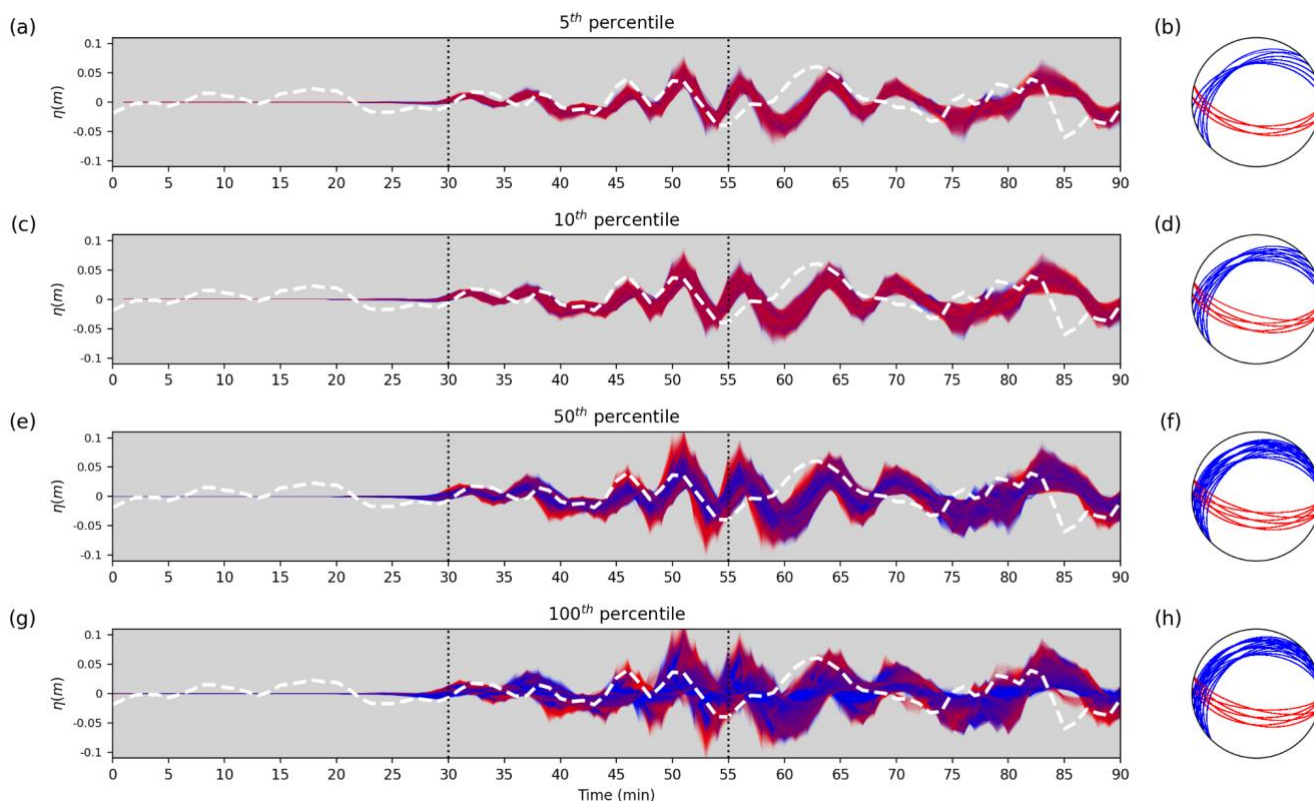
369



370
371 **Figure 9** From top to bottom, the left-hand side panels (a, c, e, g) show the marigrams of the events, ordered by cost function value,
372 corresponding to the 5th, 10th, 50th, and 100th percentiles. The white dashed line is the observed water elevation at the Ierapetra tide-gauge



373 (NOA-04). The vertical dotted lines indicate the limits of the time window used for the inversion. The stereonets (lower hemisphere) on the
374 right-hand side (b, d, f, h) show the fault plane variability corresponding to the synthetic waveforms. Red and blue refer to plane B (back-
375 thrust solutions) and plane S (splay fault solutions), respectively, both for waveforms and fault planes.



376
377 **Figure 10:** The same as Figure 9 but for the Kasos tide-gauge (NOA-03) signal.

378 **4 Discussion**

379 We constrained the source model of the 2020 Cretan Passage earthquake (Mw 6.6) by comparing the sea level observations at
380 two tide-gauges with the synthetic tsunami waveforms.

381 We could use only one tsunami record not too distant from the source and one farther away. The availability of more
382 instruments would be precious for both real-time operations and event characterisation. Moreover, a better characterisation of
383 harbour response and the implementation in the future of high-resolution in-harbour propagation could be important,
384 particularly considering that deep-sea instruments are nearly absent in the Mediterranean Sea.

385
386 We compared the waveforms generated with our solutions with those we simulated using two different source models already
387 published for the 2020 Cretan Passage tsunami: the one presented by Wang et al. (2020; “W” model hereafter), who use the



388 event as a test-case for a hypothetical offshore bottom pressure gauges network around Crete Island, to assist tsunami early
389 warning through real data assimilation, and the Heidarzadeh and Gusman (2021) model (“HG” model hereafter), obtained by
390 inversion of the same tsunami dataset we used in this study.

391
392 Figure 11 displays the marigrams calculated with our preferred models together with the waveforms generated by W and HG
393 models. The W waveform tends to overestimate the observed signal, both at Ierapetra and Kasos tide-gauge. The HG waveform
394 reproduces well the observed signal at the Ierapetra station, while it overestimates the signal around minute 50 at Kasos. The
395 cost functions associated with the four models, evaluated as described in Section 2, are 0.097, 0.104, 0.583, 0.253 for our B
396 and S planes and for W and HG models, respectively. Using these values, and assuming a rigidity of 33 GPa, consistently with
397 Leonard (2014)’s scaling relationships, the seismic moment associated with the four source models is 6.63, 7.29, 11.9, 11.1
398 ($\times 10^{18}$) Nm, corresponding to Mw 6.5, 6.6, 6.7, and 6.7, respectively.

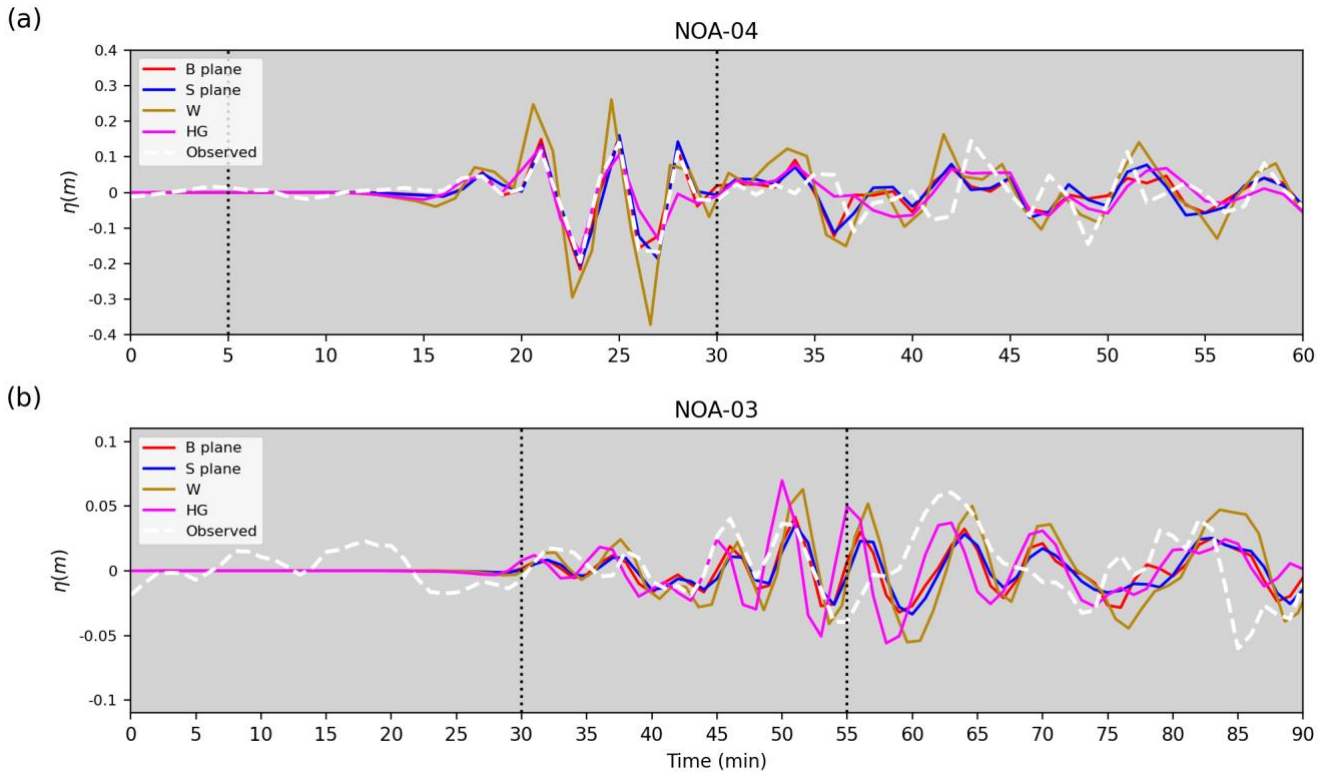
399
400 The W model, whose waveform presents the largest misfit, consists of a single fault (20 km \times 12 km) with a uniform slip of
401 1.5 m. The epicentre is at 34.205°N, 25.712°E, and the top depth of the fault is 11.5 km; strike, dip, and rake angles are 229°,
402 31°, and 46°, respectively. These parameters are based on the W-phase focal mechanism solution of the USGS. The slip value
403 is significantly larger than in our preferred models, and it can explain the overestimation. When the same source is used by
404 Wang et al. (2020; see their Figure 9), the agreement between the synthetic and observed waveforms is better. However, Wang
405 et al. (2020) used a bathymetric grid with a resolution of 30 arcsec (\sim 925 m), while we used a nested grid approach with a
406 resolution up to 10 m around the tide-gauge positions (see Section 2). This likely guarantees a better convergence of the
407 numerical simulation of the relatively short wavelengths characterising this tsunami and explains the difference. When using
408 a lower resolution, the waveforms can only be reproduced by artificially increasing the fault slip. The role of accurate
409 bathymetry is of fundamental importance to ensure accurate tsunami simulations also for source characterisation.

410
411 The HG model, with assigned location and focal mechanism (reported in the Introduction), presents a source dimension of
412 40 \times 30 km and a heterogeneous slip distribution with a maximum slip of 0.64 m and an average slip of 0.28 m. In this case,
413 high-resolution modelling is used around the tide-gauges as well. The slip value of our sources is quite larger than their average,
414 but associated with a smaller fault (see Table 1). The overall higher cost function value for the HG model retrieved with our
415 setup can be explained by the fact that the inversion time windows are 13 and 10 minutes for Ierapetra and Kasos tide-gauges,
416 respectively, much shorter than the ones used in this study (Section 2).

417
418
419
420
421



422



423

424

425

426

Figure 11: Waveforms obtained at the Ierapetra NOA-04 (a) and Kasos NOA-03 (b) tide-gauges by the best source models of the back-thrust solution (the B plane in red), the best of the splay fault solution (the S plane in blue), the fault defined by Wang et al. (2020) and the one by Heidarzadeh and Gusman (2021). The vertical dotted lines indicate the limits of the time window used for the inversion.

427

428

429

430

431

432

433

434

435

436

437

438

Starting from the available focal mechanisms, we explored two thrust faulting solutions (Figure 12), a north-dipping reverse splay fault (plane S) and a south-dipping back-thrust (plane B). We found a slightly better agreement for the waveforms corresponding to the B plane with respect to those of the S plane (Figure 4). However, this difference is not big enough to draw a strong conclusion concerning the causative fault of this earthquake.

Despite this ambiguity between the two fault planes (S and B), still important considerations emerge from this study. Both solutions seem shallow enough to indicate that the earthquake was embedded within the inner parts of the HASZ accretionary wedge, thus excluding either a subduction interface or intraslab earthquake. In particular, the strike of the B plane and the dip of the S plane contribute to excluding a subduction interface earthquake.

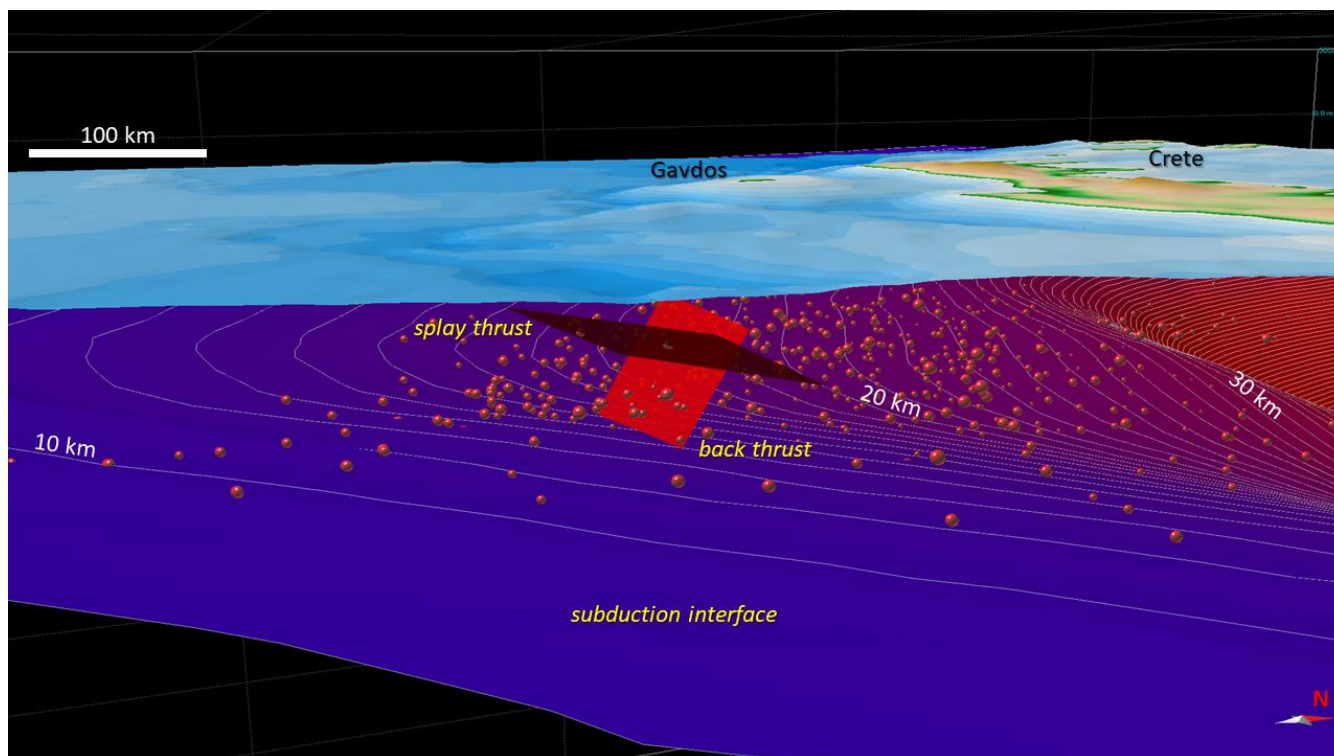


439 From the geological viewpoint, plane B could represent a back-thrust fault accommodating the contraction of the inner parts
440 of the Mediterranean Ridge against the Cretan backstop. This south-eastern Cretan margin is surrounded by the double Pliny
441 and Strabo trenches system, which have been related to back-thrust fault activity (Camerlenghi et al., 1992; Leite and Mascle,
442 1982; Chaumillon and Mascle, 1997). Back-thrusting is considered to be the cause of the formation of a topographic
443 escarpment separating the wedge from the Inner Ridge backstop (Kopf et al., 2003). The plane S could represent the
444 reactivation of one of the thrusts marking the advancement of the deformation front within the accretionary wedge above the
445 main decollement or a splay fault emanating directly from the subduction interface.

446
447 In either case, the orientation of the fault plane and the slip direction are compatible with the long-term kinematic indicators.
448 Within the region of the HASZ where the Cretan Passage earthquake occurred, in fact, the average direction of convergence
449 is $\sim 200\text{-}220^\circ$ from GPS velocity data (Reilinger et al., 2006; Floyd et al., 2010; Noquet, 2012) and the azimuth of the maximum
450 horizontal stress (SHmax) is $0\text{-}20^\circ$ (Carafa and Barba, 2013). The splay fault S features a small left-lateral slip component,
451 which is consistent with the increasingly oblique convergence in the eastern branch of the HASZ (Bohnhoff et al., 2005;
452 Yolsal-Çevikbilen and Taymaz, 2012).

453
454 The combination of the shallow depth and the high dip angle plays a key role in determining the tsunamigenic potential
455 associated with the fault. The steeper dip angle and the shallower depth tend to produce a vertical deformation whose
456 tsunamigenic potential is more pronounced than that induced by the very low-angle interface earthquakes of similar magnitude.
457 Note, however, that the dip angle of the two proposed solutions is higher than those derived from seismic reflection profiles
458 for these types of thrust faults in the region (Kopf et al., 2003).

459
460 For example, the moderate earthquake of $M_w = 6.45$, which occurred on July 1, 2009 (Bocchini et al., 2020), was the cause of
461 a local tsunami because it ruptured in the overriding crust as for the 2020 Cretan Passage earthquake. Conversely, other larger
462 earthquakes occurred nearby, apparently without generating a tsunami. Just focusing on the portion of the Hellenic trench
463 south of Crete, this is, for example, the case of the $M_s 7$, December 17, 1952, earthquake occurred at a depth of about 25 km
464 (Papazachos, 1996), and the $M_s 6.5$, May 4, 1972, earthquake occurred at ~ 40 km depth (Kiritzi and Langston, 1989).



465

466

467

Figure 12: Oblique view, looking westward, of the fault planes obtained in this study and their relation with the subduction interface shown by depth contours (white lines) and the aftershock seismicity (red spheres) until 18/04/2021.

468

5 Conclusions

469

470

471

472

473

474

475

476

477

478

479

480

481

We investigated the seismic fault structure and the rupture characteristics of the Mw 6.6, May 2, 2020, Cretan Passage earthquake through tsunami data inverse modelling. Our results confirm the indication from moment tensor solutions that this was a shallow crustal event with a reverse mechanism within the accretionary wedge rather than on the Hellenic Arc subduction interface.

Using two marigrams, only one of which in the near field with respect to the seismic source, we could highlight important characteristics of this earthquake, especially from a tsunamigenesis perspective, although the adopted method and the limited data available did not prove sufficient to isolate the main focal plane. The sea-level heights recorded at Ierapetra and Kasos tide-gauges identify two possible ruptures: a steeply sloping reverse splay fault and a back-thrust rupture dipping south, with a more prominent dip angle. The a-posteriori appraisal of the ensemble of models tested allows for a slight preference for the south-dipping back-thrust over the splay fault.

Nevertheless, both are high-angle reverse faults in the upper plate above the plate interface with a tsunamigenic potential higher than that of interplate earthquakes of similar or even slightly larger moment magnitude.



482

483 This is important for seismic and tsunami hazard assessment, since the presence of shallow crustal ruptures should not be
484 overlooked in an area where subduction interface (interplate) events are also possible. Note that, for example, the recent
485 NEAMTHM18 tsunami hazard model considered the possibility of crustal faults rupturing everywhere in the overriding plate
486 (Basili et al., 2021).

487

488 Although the tsunami did not cause damages or victims, the event represents yet another testimony of how such events are
489 frequent and typical in the Mediterranean and, particularly, along the Hellenic arc. In addition to this, the near-source nature
490 of the event should be emphasised. Despite the improvements and developments carried out by the NEAMTWS Tsunami
491 Service Providers in recent years, that have proven to be capable of issuing tsunami messages within 10 minutes after the
492 earthquake origin time (Amato et al., 2021), the early tsunami arrival (tenths of minutes or less) at the closest coasts leaves
493 very little time for warning, which is probably the case in many regions in the world. Then, together with an efficient warning
494 system, education, awareness and preparation remain by far the most cost-effective investments for local tsunamis (Imamura
495 et al., 2019). The 2020 Cretan Passage earthquake is another reminder of the tsunami risk in the Mediterranean Sea, but also
496 of the fact that it is extremely appropriate to promptly react to felt shaking, since also moderate earthquakes that are shallow
497 and occur on steep faults may generate a significant and dangerous tsunami.

498

499 *Acknowledgements.* The research reported in this work was supported by OGS and CINECA under HPC-TRES program award
500 number 2020-01, and co-funded by the Italian flagship project RITMARE. RB acknowledges the resources made available by
501 the SISMOLAB-3D at INGV.

502 **References**

- 503 Amante, C., and Eakins, B. W. (2009). ETOPO1 1 arc-minute global relief model: procedures, data sources and analysis.
504 NOAA technical memorandum NESDIS NGDC-24. National Geophysical Data Center, NOAA.
505 doi:10.7289/V5C8276M, 2009, last access: 5, 2020.
- 506 Amato, A., Avallone, A., Basili, R., Bernardi, F., Brizuela, B., Graziani, L., Herrero, A., Lorenzino, M. C., Lorito, S., Mele,
507 F. M., Michelini, A., Piatanesi, A., Pintore, S., Romano, F., Selva, J., Stramondo, S., Tonini, R., and Volpe, M.: From
508 Seismic Monitoring to Tsunami Warning in the Mediterranean Sea, *Seism. Res. Lett.*, 92, 1796–1816,
509 <https://doi.org/10.1785/0220200437>, 2021.
- 510 Basili, R., Kastelic, V., Demircioglu, M. B., Garcia Moreno, D., Nemser, E. S., Petricca, P., Sboras, S. P., Besana-Ostman, G.
511 M., Cabral, J., Camelbeeck, T., Caputo, R., Danciu, L., Domaç, H., Fonseca, J. F. de B. D., García-Mayordomo, J.,
512 Giardini, D., Glavatovic, B., Gulen, L., Ince, Y., Pavlides, S., Sesetyan, K., Tarabusi, G., Tiberti, M. M., Utkucu, M.,
513 Valensise, G., Vanneste, K., Vilanova, S. P., and Wössner, J.: European Database of Seismogenic Faults (EDSF)



- 514 compiled in the framework of Project SHARE,, <https://doi.org/10.6092/INGV.IT-SHARE-EDSF>, 2013, last access:
515 May 31, 2021.
- 516 Basili, R., Brizuela, B., Herrero, A., Iqbal, S., Lorito, S., Maesano, F. E., Murphy, S., Perfetti, P., Romano, F., Scala, A., Selva,
517 J., Taroni, M., Tiberti, M. M., Thio, H. K., Tonini, R., Volpe, M., Glimsdal, S., Harbitz, C. B., Løvholt, F., Baptista,
518 M. A., Carrilho, F., Matias, L. M., Omira, R., Babeyko, A., Hoechner, A., Gürbüz, M., Pekcan, O., Yalçın, A., Canals,
519 M., Lastras, G., Agalos, A., Papadopoulos, G., Triantafyllou, I., Benchekroun, S., Agrebi Jaouadi, H., Ben Abdallah,
520 S., Bouallegue, A., Hamdi, H., Oueslati, F., Amato, A., Armigliato, A., Behrens, J., Davies, G., Di Bucci, D., Dolce,
521 M., Geist, E., Gonzalez Vida, J. M., González, M., Macías Sánchez, J., Meletti, C., Ozer Sozdinler, C., Pagani, M.,
522 Parsons, T., Polet, J., Power, W., Sørensen, M., and Zaytsev, A.: The Making of the NEAM Tsunami Hazard Model
523 2018 (NEAMTHM18), *Front. Earth Sci.*, 8, 753, <https://doi.org/10.3389/feart.2020.616594>, 2021.
- 524 Bocchini, G. M., Novikova, T., Papadopoulos, G. A., Agalos, A., Mouzakiotis, E., Karastathis, V., and Voulgaris, N.: Tsunami
525 Potential of Moderate Earthquakes: The July 1, 2009 Earthquake (Mw 6.45) and its Associated Local Tsunami in the
526 Hellenic Arc, *Pure Appl. Geophys.*, 177, 1315–1333, <https://doi.org/10.1007/s00024-019-02246-9>, 2020.
- 527 Bohnhoff, M., Harjes, H.-P., and Meier, T.: Deformation and stress regimes in the Hellenic subduction zone from focal
528 Mechanisms, *J. Seismol.*, 9, 341–366, <https://doi.org/10.1007/s10950-005-8720-5>, 2005.
- 529 Camerlenghi, A., Cita, M. B., Hieke, W., and Ricchiuto, T.: Geological evidence for mud diapirism on the Mediterranean
530 Ridge accretionary complex, *Earth and Planetary Sci. Lett.*, 109, 493–504, [https://doi.org/10.1016/0012-821X\(92\)90109-9](https://doi.org/10.1016/0012-821X(92)90109-9), 1992.
- 532 Carafa, M. M. C. and Barba, S.: The stress field in Europe: optimal orientations with confidence limits, *Geophys. J. Int.*, 193,
533 531–548, <https://doi.org/10.1093/gji/ggt024>, 2013.
- 534 Chamot-Rooke, N., Rabaute, A., and Kreemer, C.: Western Mediterranean Ridge mud belt correlates with active shear strain
535 at the prism-backstop geological contact, *Geology*, 33, 861–864, <https://doi.org/10.1130/G21469.1>, 2005.
- 536 Chaumillon, E. and Mascle, J.: From foreland to forearc domains: New multichannel seismic reflection survey of the
537 Mediterranean ridge accretionary complex (Eastern Mediterranean), *Marine Geology*, 138, 237–259,
538 [https://doi.org/10.1016/S0025-3227\(97\)00002-9](https://doi.org/10.1016/S0025-3227(97)00002-9), 1997.
- 539 Cirella, A., Romano, F., Avallone, A., Piatanesi, A., Briole, P., Ganas, A., Theodoulidis, N., Chousianitis, K., Volpe, M.,
540 Bozionellos, G., Selvaggi, G., and Lorito, S.: The 2018 Mw 6.8 Zakynthos (Ionian Sea, Greece) earthquake: seismic
541 source and local tsunami characterization, *Geophys. J. Int.*, 221, 1043–1054, <https://doi.org/10.1093/gji/ggaa053>, 2020.
- 542 De la Asunción, M., Castro, M. J., Fernández-Nieto, E. D., Mantas, J. M., Acosta, S. O., and González-Vida, J. M.: Efficient
543 GPU implementation of a two waves TVD-WAF method for the two-dimensional one layer shallow water system on
544 structured meshes, *Computers & Fluids*, 80, 441–452, <https://doi.org/10.1016/j.compfluid.2012.01.012>, 2013.
- 545 Dzierwonski, A. M., Chou, T.-A., and Woodhouse, J. H.: Determination of earthquake source parameters from waveform data
546 for studies of global and regional seismicity, *J. Geophys. Res.: Solid Earth*, 86, 2825–2852,
547 <https://doi.org/10.1029/JB086iB04p02825>, 1981.



- 548 Ekström, G., Nettles, M., and Dziewoński, A. M.: The global CMT project 2004–2010: Centroid-moment tensors for 13,017
549 earthquakes, *Physics of the Earth and Planetary Interiors*, 200–201, 1–9, <https://doi.org/10.1016/j.pepi.2012.04.002>,
550 2012.
- 551 EMODnet Bathymetry Consortium, EMODnet Digital Bathymetry (DTM), 2020, available online at:
552 <https://doi.org/10.12770/bb6a87dd-e579-4036-abe1-e649cea9881a>, 2020, last access March 20, 2021.
- 553 Floyd, M. A., Billiris, H., Paradissis, D., Veis, G., Avallone, A., Briole, P., McClusky, S., Nocquet, J.-M., Palamartchouk, K.,
554 Parsons, B., and England, P. C.: A new velocity field for Greece: Implications for the kinematics and dynamics of the
555 Aegean, *J. Geophys. Res.: Solid Earth*, 115, <https://doi.org/10.1029/2009JB007040>, 2010.
- 556 Grünthal, G. and Wahlström, R.: The European-Mediterranean Earthquake Catalogue (EMEC) for the last millennium, *J.*
557 *Seismol.*, 16, 535–570, <https://doi.org/10.1007/s10950-012-9302-y>, 2012.
- 558 Guidoboni, E. and Comastri, A.: The large earthquake of 8 August 1303 in Crete: seismic scenario and tsunami in the
559 Mediterranean area, *J. Seismol.*, 1, 55–72, <https://doi.org/10.1023/A:1009737632542>, 1997.
- 560 Heidarzadeh, M. and Gusman, A. R.: Source modeling and spectral analysis of the Crete tsunami of 2nd May 2020 along the
561 Hellenic Subduction Zone, offshore Greece, *Earth, Planets and Space*, 73, 1-16, [https://doi.org/10.1186/s40623-021-](https://doi.org/10.1186/s40623-021-01394-4)
562 01394-4, 2021.
- 563 Kajiura, K.: The leading wave of a tsunami, *Bull. Earthquake Res. Inst. Univ., Tokyo*, 41, 535–571, 1963..
- 564 Kastens, K. A.: Rate of outward growth of the Mediterranean ridge accretionary complex, *Tectonophysics*, 199, 25–50,
565 [https://doi.org/10.1016/0040-1951\(91\)90117-B](https://doi.org/10.1016/0040-1951(91)90117-B), 1991.
- 566 Kiratzi, A. A. and Langston, C. A.: Estimation of earthquake source parameters of the May 4, 1972 event of the Hellenic arc
567 by the inversion of waveform data, *Physics of the Earth and Planetary Interiors*, 57, 225–232,
568 [https://doi.org/10.1016/0031-9201\(89\)90113-1](https://doi.org/10.1016/0031-9201(89)90113-1), 1989.
- 569 Kopf, A., Mascle, J., and Klaeschen, D.: The Mediterranean Ridge: A mass balance across the fastest growing accretionary
570 complex on Earth, *J. Geophys. Res.: Solid Earth*, 108, <https://doi.org/10.1029/2001JB000473>, 2003.
- 571 Imamura, F., Boret, S. P., Suppasri, A., and Muhari, A.: Recent occurrences of serious tsunami damage and the future
572 challenges of tsunami disaster risk reduction, *Progress in Disaster Science*, 1, 100009,
573 <https://doi.org/10.1016/j.pdisas.2019.100009>, 2019.
- 574 Leite, O. and Mascle, J.: Geological structures on the South Cretan continental margin and Hellenic Trench (eastern
575 Mediterranean), *Marine Geology*, 49, 199–223, [https://doi.org/10.1016/0025-3227\(82\)90040-8](https://doi.org/10.1016/0025-3227(82)90040-8), 1982.
- 576 Leonard, M.: Self-Consistent Earthquake Fault-Scaling Relations: Update and Extension to Stable Continental Strike-Slip
577 FaultsSelf-Consistent Earthquake Fault-Scaling Relations, *Bull. Seism. Soc. Am.*, 104, 2953–2965,
578 <https://doi.org/10.1785/0120140087>, 2014.
- 579 Macías, J., Castro, M. J., Ortega, S., Escalante, C., and González-Vida, J. M.: Performance Benchmarking of Tsunami-HySEA
580 Model for NTHMP's Inundation Mapping Activities, *Pure Appl. Geophys.*, 174, 3147–3183,
581 <https://doi.org/10.1007/s00024-017-1583-1>, 2017.



- 582 Mosegaard, K. and Tarantola, A.: Monte Carlo sampling of solutions to inverse problems, *J. Geophys. Res.: Solid Earth*, 100,
583 12431–12447, <https://doi.org/10.1029/94JB03097>, 1995.
- 584 NOAA National Geophysical Data Center, ETOPO1 1 arc-minute global relief model. NOAA National Centers for
585 Environmental Information, 2009. available at: <https://www.ngdc.noaa.gov/mgg/global/>, last Access December 5,
586 2020.
- 587 Nocquet, J.M.: Present-day kinematics of the Mediterranean: A comprehensive overview of GPS results, *Tectonophysics*, 579,
588 220–242, <https://doi.org/10.1016/j.tecto.2012.03.037>, 2012.
- 589 Okada, Y.: Internal deformation due to shear and tensile faults in a half-space, *Bull. Seism. Soc. Am.*, 82, 1018–1040, 1992.
- 590 Ott, R. F., Wegmann, K. W., Gallen, S. F., Pazzaglia, F. J., Brandon, M. T., Ueda, K., and Fassoulas, C.: Reassessing Eastern
591 Mediterranean Tectonics and Earthquake Hazard From the 365 CE Earthquake, *AGU Advances*, 2, e2020AV000315,
592 <https://doi.org/10.1029/2020AV000315>, 2021.
- 593 Papadopoulos, G. A., Daskalaki, E., Fokaefs, A., and Giraleas, N.: Tsunami hazards in the Eastern Mediterranean: strong
594 earthquakes and tsunamis in the East Hellenic Arc and Trench system, *Nat. Hazards Earth Syst. Sci.*, 7, 57–64,
595 <https://doi.org/10.5194/nhess-7-57-2007>, 2007.
- 596 Papadopoulos G. A. A Seismic history of Crete: earthquakes and tsunamis, 2000 BC – 2011 AD. Athens: Ocelotos
597 Publications; 2011.
- 598 Papadopoulos, G. A., Gràcia, E., Urgeles, R., Sallares, V., De Martini, P. M., Pantosti, D., González, M., Yalciner, A. C.,
599 Mascle, J., Sakellariou, D., Salamon, A., Tinti, S., Karastathis, V., Fokaefs, A., Camerlenghi, A., Novikova, T., and
600 Papageorgiou, A.: Historical and pre-historical tsunamis in the Mediterranean and its connected seas: Geological
601 signatures, generation mechanisms and coastal impacts, *Marine Geology*, 354, 81–109,
602 <https://doi.org/10.1016/j.margeo.2014.04.014>, 2014.
- 603 Papadopoulos, G. A., Lekkas, E., Katsetsiadou, K.-N., Rovythakis, E., and Yahav, A.: Tsunami Alert Efficiency in the Eastern
604 Mediterranean Sea: The 2 May 2020 Earthquake (Mw6.6) and Near-Field Tsunami South of Crete (Greece),
605 *GeoHazards*, 1, 44–60, <https://doi.org/10.3390/geohazards1010005>, 2020.
- 606 Papazachos, B. S.: Large seismic faults in the Hellenic arc, *Annali di Geofisica*, 39, <https://doi.org/10.4401/ag-4023>,
607 1996.
- 608 Papazachos, B. and Papazachos, C.: Accelerated Preshock Deformation of Broad Regions in the Aegean Area, *Pure appl.*
609 *geophys.*, 157, 1663–1681, <https://doi.org/10.1007/PL00001055>, 2000.
- 610 Papazachos, B. C., Karakaisis, G. F., Papazachos, C. B., and Scordilis, E. M.: Earthquake triggering in the North and East
611 Aegean Plate Boundaries due to the Anatolia Westward Motion, *Geophys. Res. Lett.*, 27, 3957–3960,
612 <https://doi.org/10.1029/2000GL011425>, 2000.
- 613 Piatanesi, A. and Lorito, S.: Rupture Process of the 2004 Sumatra–Andaman Earthquake from Tsunami Waveform Inversion,
614 *Bull. Seism. Soc. Am.*, 97, S223–S231, <https://doi.org/10.1785/0120050627>, 2007.
- 615 Polonia, A., Camerlenghi, A., Davey, F., and Storti, F.: Accretion, structural style and syn-contractional sedimentation in the



- 616 Eastern Mediterranean Sea, *Marine Geology*, 186, 127–144, [https://doi.org/10.1016/S0025-3227\(02\)00176-7](https://doi.org/10.1016/S0025-3227(02)00176-7), 2002.
- 617 Reilinger, R., McClusky, S., Vernant, P., Lawrence, S., Ergintav, S., Cakmak, R., Ozener, H., Kadirov, F., Guliev, I.,
618 Stepanyan, R., Nadariya, M., Hahubia, G., Mahmoud, S., Sakr, K., ArRajehi, A., Paradissis, D., Al-Aydrus, A., Prilepin,
619 M., Guseva, T., Evren, E., Dmitrotsa, A., Filikov, S. V., Gomez, F., Al-Ghazzi, R., and Karam, G.: GPS constraints on
620 continental deformation in the Africa-Arabia-Eurasia continental collision zone and implications for the dynamics of
621 plate interactions, *J. Geophys. Res.: Solid Earth*, 111, <https://doi.org/10.1029/2005JB004051>, 2006.
- 622 Romano, F., Molinari, I., Lorito, S., and Piatanesi A.: Source of the 6 February 2013 Mw = 8.0 Santa Cruz Islands Tsunami,
623 *Nat. Hazards Earth Syst. Sci.*, 15, 1371–1379, doi:10.5194/nhess-15-1371-2015, 2015.
- 624 Romano, F., Piatanesi, A., Lorito, S., Tolomei, C., Atzori, S., and Murphy, S.: Optimal time alignment of tide-gauge tsunami
625 waveforms in nonlinear inversions: Application to the 2015 Illapel (Chile) earthquake, *Geophys. Res. Lett.*, 43, 11,226-
626 11,235, <https://doi.org/10.1002/2016GL071310>, 2016.
- 627 Romano, F., Lorito, S., Lay, T., Piatanesi, A., Volpe, M., Murphy, S., and Tonini, R.: Benchmarking the Optimal Time
628 Alignment of Tsunami Waveforms in Nonlinear Joint Inversions for the Mw 8.8 2010 Maule (Chile) Earthquake, *Front.*
629 *Earth Sci.*, 8, <https://doi.org/10.3389/feart.2020.585429>, 2020.
- 630 Saltogianni, V., Mouslopoulou, V., Oncken, O., Nicol, A., Gianniou, M., and Mertikas, S.: Elastic Fault Interactions and
631 Earthquake Rupture Along the Southern Hellenic Subduction Plate Interface Zone in Greece, *Geophys. Res. Lett.*, 47,
632 e2019GL086604, <https://doi.org/10.1029/2019GL086604>, 2020.
- 633 Sambridge, M. and Mosegaard, K.: Monte Carlo Methods in Geophysical Inverse Problems, 40, 3-1-3–29, *Rev. geophys.*,
634 <https://doi.org/10.1029/2000RG000089>, 2002.
- 635 Shaw, B., Ambraseys, N. N., England, P. C., Floyd, M. A., Gorman, G. J., Higham, T. F. G., Jackson, J. A., Nocquet, J.-M.,
636 Pain, C. C., and Piggott, M. D.: Eastern Mediterranean tectonics and tsunami hazard inferred from the AD 365
637 earthquake, *Nat. Geosci.*, 1, 268–276, <https://doi.org/10.1038/ngeo151>, 2008.
- 638 Shaw, B. and Jackson, J.: Earthquake mechanisms and active tectonics of the Hellenic subduction zone, *Geophys. J. Int.*, 181,
639 966–984, <https://doi.org/10.1111/j.1365-246X.2010.04551.x>, 2010.
- 640 Sørensen, M. B., Spada, M., Babeyko, A., Wiemer, S., and Grünthal, G.: Probabilistic tsunami hazard in the Mediterranean
641 Sea, *J. Geophys. Res.: Solid Earth*, 117, <https://doi.org/10.1029/2010JB008169>, 2012.
- 642 Stiros, S. C.: The AD 365 Crete earthquake and possible seismic clustering during the fourth to sixth centuries AD in the
643 Eastern Mediterranean: a review of historical and archaeological data, *J. of Structural Geology*, 23, 545–562,
644 [https://doi.org/10.1016/S0191-8141\(00\)00118-8](https://doi.org/10.1016/S0191-8141(00)00118-8), 2001.
- 645 Stucchi, M., Rovida, A., Gomez Capera, A. A., Alexandre, P., Camelbeeck, T., Demircioglu, M. B., Gasperini, P., Kouskouna,
646 V., Musson, R. M. W., Radulian, M., Sesetyan, K., Vilanova, S., Baumont, D., Bungum, H., Fäh, D., Lenhardt, W.,
647 Makropoulos, K., Martinez Solares, J. M., Scotti, O., Živčić, M., Albini, P., Batllo, J., Papaioannou, C., Tatevossian,
648 R., Locati, M., Meletti, C., Viganò, D., and Giardini, D.: The SHARE European Earthquake Catalogue (SHEEC) 1000–
649 1899, *J. Seismol.*, 17, 523–544, <https://doi.org/10.1007/s10950-012-9335-2>, 2013.



- 650 Synolakis, C. E., Bernard, E. N., Titov, V. V., Kânoğlu, U., and González, F. I.: Validation and Verification of Tsunami
651 Numerical Models, in: *Tsunami Science Four Years after the 2004 Indian Ocean Tsunami: Part I: Modelling and Hazard*
652 *Assessment*, edited by: Cummins, P. R., Satake, K., and Kong, L. S. L., Birkhäuser, Basel, 2197–2228,
653 https://doi.org/10.1007/978-3-0346-0057-6_11, 2009.
- 654 Tarantola, A.: Inversion of travel times and seismic waveforms, in: *Seismic Tomography: With Applications in Global*
655 *Seismology and Exploration Geophysics*, edited by: Nolet, G., Springer Netherlands, Dordrecht, 135–157,
656 https://doi.org/10.1007/978-94-009-3899-1_6, 1987.
- 657 Wang, Y., Heidarzadeh, M., Satake, K., Mulia, I. E., and Yamada, M.: A Tsunami Warning System Based on Offshore Bottom
658 Pressure Gauges and Data Assimilation for Crete Island in the Eastern Mediterranean Basin, *J. Geophys. Res.: Solid*
659 *Earth*, 125, e2020JB020293, <https://doi.org/10.1029/2020JB020293>, 2020.
- 660 Woessner, J., Laurentiu, D., Giardini, D., Crowley, H., Cotton, F., Grünthal, G., Valensise, G., Arvidsson, R., Basili, R.,
661 Demircioglu, M. B., Hiemer, S., Meletti, C., Musson, R. W., Rovida, A. N. and Sesetyan, K. and Stucchi, M., and The
662 SHARE Consortium : The 2013 European seismic hazard model : key components and results, *Bull. of Earthquake*
663 *Eng.*, 13, 3553–3596, <https://doi.org/10.1007/s10518-015-9795-1>, 2015.
- 664 Yem, L. M., Camera, L., Mascle, J., and Ribodetti, A.: Seismic stratigraphy and deformational styles of the offshore Cyrenaica
665 (Libya) and bordering Mediterranean Ridge, *Geophys. J. Int.*, 185, 65–77, [https://doi.org/10.1111/j.1365-](https://doi.org/10.1111/j.1365-246X.2011.04928.x)
666 [246X.2011.04928.x](https://doi.org/10.1111/j.1365-246X.2011.04928.x), 2011.
- 667 Yolsal-Çevikbilen, S. and Taymaz, T.: Earthquake source parameters along the Hellenic subduction zone and numerical
668 simulations of historical tsunamis in the Eastern Mediterranean, *Tectonophysics*, 536–537, 61–100,
669 <https://doi.org/10.1016/j.tecto.2012.02.019>, 2012.